

Spectroscopy of ^{111}Cd : Challenging the particle-vibration model

Ben Coombes

A thesis submitted for the degree of
Bachelor of Science with Honours in Physics of
The Australian National University

October, 2016

Declaration

This thesis is an account of research undertaken between February 2016 and October 2016 at The Department of Physics, Faculty of Science, The Australian National University, Canberra, Australia.

Except where acknowledged in the customary manner, the material presented in this thesis is, to the best of my knowledge, original and has not been submitted in whole or part for a degree in any university.

Ben Coombes
October, 2016

Acknowledgements

Appreciation is owed to many people for assistance throughout my year at the Department of Nuclear Physics. Particular thanks go to my supervisor Andrew Stuchbery for giving up so much of his time to explain concepts of nuclear structure and the techniques used in data analysis. Without him this thesis would never have been completed. Gratitude also is given to Matt Reed for his input in the experimental week. The consistency of Matt's presence during the experimental run was noted and appreciated. I would also like to recognise the technical staff, A.J. Mitchell, and the other students in the department for giving up their time to run the accelerator, it would have been a long week on my own. Thanks are also due to Tibor Kibédi for the provision of analysis programs used in this work and his time spent modifying FITEK for my needs. My thanks also goes to Claes Fahlander for the time spent teaching me to run the GOSIA code.

To my family endless appreciation is given for their willingness to listen to my stressed rants. I will always be grateful for the time you spent to raise me and the opportunities I have been provided at university. The support you have given me throughout my years at the ANU has been essential.

Thanks are also due to my flatmates for cooking me meals for the last week, and allowing me to focus on my thesis. The food has been greatly appreciated.

Finally, to my partner Zofia, the encouragement and reassurance you have provided cannot be understated. Thank you.

Much of the analysis in this thesis relies heavily on programs written by members of the department. Sorting and fitting procedures were performed using TSORT and FITEK provided by Tibor Kibédi. The programs used for calculation of the statistical tensors and hence the angular distributions are based on the de Boer-Winther code and were written and provided by Andrew Stuchbery.

Abstract

In this thesis the structure of ^{111}Cd is explored through measurement of spectroscopic observables. Coulomb excitation was performed using a beam of ^{32}S from the Australian National University (ANU) 14UD tandem pelletron accelerator. Low-lying states in ^{111}Cd were excited and angular correlation measurements were performed for several states. These measurements allowed clarification of inconsistencies in the literature surrounding $\frac{5}{2}^{+}$ and $\frac{3}{2}^{+}$ states at 752.8 keV and 754.9 keV, respectively. Previous studies of ^{111}Cd had individually seen only a single state around this energy. In this work one state is observed at 752.8 keV and a pure $E2$ transition between this state and the $\frac{1}{2}^{+}$ ground state confirms the $\frac{5}{2}^{+}$ spin assignment.

Traditionally the even-even Cd isotopes have been cited in textbooks as vibrational nuclei. Recent measurements of transition strengths between excited states previously believed to have been from quadrupole surface vibrations have cast doubts on this model. This thesis investigates the odd- A nucleus ^{111}Cd in which an odd neutron is coupled to the even-even core excitations. In effect the odd neutron serves to probe the excitations of the core. In order to study the nature of ^{111}Cd , measurements of the g factors for excited states were performed using the ANU hyperfine spectrometer and compared with the particle-vibration model which couples the odd nucleon to a vibrational core. Significant disagreement was found between the experimentally determined g factors and the particle-vibration model. Another significant issue for the particle-vibrator description of this nucleus is the lack of a predicted second, strongly Coulomb excited, $\frac{3}{2}^{+}$ state from the coupling of the $\frac{1}{2}^{+}$ ground state to the 2^{+} core excitation. An alternative explanation for the low-lying states observed in ^{111}Cd is offered in terms of Nilsson orbits in the particle-rotor model.

Contents

Declaration	iii
Acknowledgements	v
Abstract	vii
1 Introduction	1
2 Nuclear structure	3
2.1 Shell model	3
2.2 Nilsson orbits and state mixing	5
2.3 Collective excitations	6
2.3.1 The harmonic vibrator model	6
2.3.2 Rotational excitations	9
2.3.3 The particle-vibrator model	11
2.3.4 Theoretical particle-vibration calculations	12
2.3.5 The particle-rotor model	12
2.4 Electromagnetic moments of nuclei	13
2.4.1 Electric quadrupole moments	13
2.4.2 Magnetic moments and g factors	14
3 Nuclear spectroscopy	17
3.1 Transitions	17
3.2 Isomeric states and decay curves	18
3.3 Example: The decay and g factor of the $\frac{5}{2}^+$ state in ^{111}Cd	19
3.4 Angular distributions and correlations	20
3.5 Mixed transitions	23
3.6 Magnetic perturbation of angular correlations	23
3.7 Model-dependant transition strength comparison	24
3.7.1 Weak-coupling model	24
3.7.2 Particle-rotor model	26
4 Previous ^{111}Cd and ^{113}Cd results	27

5	Thin-foil IMPAC technique	31
5.1	The Transient Magnetic Field	31
5.2	The Ion Implantation Perturbed Angular Correlation (IMPAC) technique	32
5.3	Thin-foil IMPAC experiments	32
6	Experimental method	35
6.1	Target preparation	35
6.2	The ANU hyperfine spectrometer	36
6.3	Beam properties	37
6.4	Detector setup	38
6.4.1	Angular correlation gamma-ray detector setup	38
6.4.2	g -factor measurement gamma detector setup	39
6.5	Analysis electronics	39
6.6	Sorting, gating, and subtractions	42
6.7	Energy calibration and angular efficiency calibration	43
7	Observed spectra and angular correlations	45
7.1	Transitions and level structure	45
7.1.1	Observed transitions	45
7.1.2	Doppler broadening	46
7.1.3	Angular correlations	48
7.2	Lifetime curve	50
8	g factor results	51
9	Discussion and interpretation	53
9.1	Particle-vibration calculations and interpretation	53
9.1.1	Predictions of energy levels	53
9.1.2	g factor comparison	54
9.2	Particle-rotor interpretation	57
9.2.1	The ground-state band	57
9.2.2	The 245 keV and 416.7 keV levels	58
9.2.3	The 752.8 keV state	59
9.2.4	The 867 keV state	59
9.2.5	g factors and the Nilsson assignments	59
10	Conclusion	61
	Bibliography	63
	Appendices	65
A	Clebsch-Gordan coefficients	67
B	Racah W-coefficients and Wigner 6j-symbols	69

List of Figures

1.1	Comparison of the level structure of ^{111}Cd and ^{113}Cd	2
2.1	Shell model diagram	5
2.2	Nilsson scheme and ground state mixing for ^{111}Cd	7
2.3	Motion of nuclear vibrations	8
2.4	^{112}Cd comparison with predicted harmonic oscillator structure	9
2.5	Deformed rotating nucleus	11
2.6	Level scheme of an odd mass rotational nucleus	13
2.7	Schmidt diagram for magnetic moments in odd-mass nuclei	16
3.1	Previously measured decay curve for the 245 keV state	19
3.2	Angular distributions for gamma-decay subprocesses	21
3.3	Example angular distributions	22
3.4	Mixed transition angular distribution	24
4.1	Particle-vibrator vs. particle-rotor calculations for ^{113}Cd	28
5.1	Three-layered target diagram	32
6.1	Diagrams of equipment used in target preparation	36
6.2	Diagram of hyperfine spectrometer target chamber	37
6.3	Angular correlation station setup	38
6.4	Sensitivity of g -factor measurement	39
6.5	Diagram of pulse processing electronics	41
6.6	Experimental particle energy spectrum	42
6.7	Experimental particle-gamma time difference spectrum	43
7.1	Experimental gamma-ray spectrum (linear scale)	45
7.2	Experimental gamma-ray spectrum (log scale)	45
7.3	Observed level scheme comparison with Nuclear Data Sheets	46
7.4	Observed angular correlations	48
7.5	Decay curve for the 245 keV transition	50
9.1	Comparison of particle-vibration level schemes with experimental levels	53
9.2	Particle-vibration model g factors as a function of the coupling parameter ξ	54
9.3	Level scheme for the Nilsson based particle-rotor interpretation of the observed level structure	57

9.4	Particle-rotor calculation of g factors as a function of quadrupole deformation ϵ_2	58
9.5	Particle-rotor calculation of single-particle energy levels as a function of quadrupole deformation ϵ_2	59

List of Tables

2.1	Spectroscopic notation for orbital angular momentum	4
3.1	Parity of transitions between nuclear states	17
3.2	Numerically evaluated formulae for reduced transition strengths	18
3.3	Weisskopf estimates of transition strengths	18
4.1	Previous experimental g factors	29
4.2	Simple Landé addition calculations for $\frac{5}{2}^+$ states	29
4.3	Experimental $B(E2)$ values in ^{111}Cd	29
6.1	Isotopic fractions of the enriched ^{111}Cd sample	35
7.1	Observed transitions, level energies and spins taken from Nuclear Data Sheets	47
8.1	Experimental g factors in ^{111}Cd	51
9.1	Particle-vibration wavefunction breakdown for the $\frac{5}{2}^+$ 752.8 keV state . .	56

Introduction

The study of nuclear structure is a complicated problem. Although much is known from many decades of study there remain widespread disagreements in the research community about the nature of some basic nuclear excitations. In recent years much focus has been on the emergence of collective motion in nuclei as a result of the correlated motion of individual nucleons. The traditional view has been that spherical nuclei near closed shells become collective by developing surface vibrations. As the numbers of both protons and neutrons outside the closed shell increase, the nuclei become deformed and show collective rotor structures. It is the vibrational structure of nuclei that has become controversial and hotly debated [Cha11, Gar10]. In this debate particular focus has been applied to the nature of excited 0^+ states in nuclei with even numbers of protons and neutrons [Hey11, Hey83, Woo92]. Traditionally these 0^+ states have been viewed as vibrations of the spherical nucleus formed by coupling two quadrupole phonons, however studies into the electric quadrupole moments and transitions in these nuclei have shown that the predictions made by the vibrational model do not fit with experimental data. To account for these deviations anharmonicity of the vibrations and the coexistence of distinct spherical and deformed nuclear shapes are invoked.

The even cadmium isotopes, such as ^{110}Cd , ^{112}Cd , and ^{114}Cd , are at the centre of the controversy, in part because they have traditionally been cited in textbooks as primary examples of vibrational nuclei, while a detailed examination of the electromagnetic properties shows severe disagreement with the vibrational model in several important ways. This thesis focuses on the odd mass isotope ^{111}Cd which is found between the controversial even isotopes ^{110}Cd and ^{112}Cd . Recently, it has been shown that the model values for magnetic dipole moments in ^{111}Cd and ^{113}Cd are sensitive to the type of motion undergone by the nominally spherical odd mass Cd nuclei and that many features in these nuclei can be explained by a small deformation and the well established rotor model [Stu16]. In order to explore this approach more thoroughly the magnetic dipole moments of excited states in ^{111}Cd are measured and compared with the predictions of the particle-vibration model.

Of particular interest in this study are the states corresponding to coupling an odd nucleon to the lowest collective excitation of the core. The literature regarding ^{111}Cd is found to contain inconsistencies in level structure relevant to the problem. In particular, two almost degenerate states have been entered into the Nuclear Data Sheets [Bla09] at

752.8 keV and 754.9 keV, whereas previous studies into this nucleus have individually only seen one state around this energy. In ^{113}Cd , which should be similar to ^{111}Cd , only one level is seen of spin and parity $I^\pi = \frac{3}{2}^+$. Its measured g factor implies that the state structure is that of a $s_{\frac{1}{2}}$ neutron coupled to the core 2_1^+ vibration. The questions addressed in this thesis are what are the spin and parity of the state near 752.8 keV in ^{111}Cd ? What is its g factor? Is the state similar or different from the nominally equivalent excitation in ^{113}Cd ?

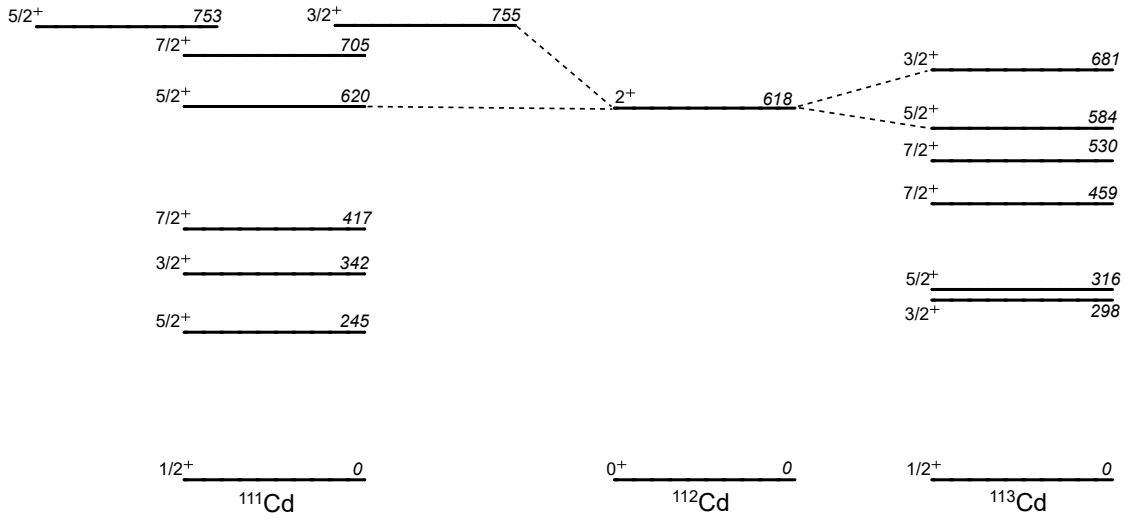


Figure 1.1: Comparison of the level structure of ^{111}Cd and ^{113}Cd . Level energy, spin and parity from Ref. [Bla09]. Dotted lines connect to the states nominally due to coupling between the odd-neutron in the $\frac{1}{2}^+$ single particle orbit and the vibrational excitation of the core.

Nuclear structure

Predictions of the properties of nuclei from a microscopic perspective are made difficult by the large number of nucleons involved (between two and several hundred) and the fact that interactions between them are not well understood. In order to investigate these properties models of nuclei are used. In this chapter the foundational models of nuclei and their predictions are discussed.

2.1 Shell model

A more fundamental approach in describing nuclear systems is to form an analogous nuclear theory to the atomic theory. Great success has been had in describing the electronic properties of atoms in terms of electrons in a central potential. The formation of an analogous nuclear theory is made more difficult by the fact that the potential acting on the nucleons is made within the nucleus by those same nucleons which establish a ‘mean field’. The fundamental assumption of the nuclear shell model is that the effective potential in which the nucleons reside can be modelled by a spherically symmetric central potential. The orbits for each particle can then be found by solving the Schrödinger equation for particles in this potential. Experimentally it is found that, similar to what is found in the atomic case, the energy required to remove a nucleon from a nucleus changes relatively smoothly as a function of the number of neutrons, or as a function of the number of protons, until rapidly increasing at so called “magic numbers” of nucleons. It is therefore reasonable to assume that a central potential approach with “shell structure” will yield results consistent with experimental results. The short range nature of the strong force would suggest that inside the nucleus the potential between nucleons would stay roughly constant before rapidly decreasing as it approaches the radius of the nucleus. A common potential to model this behaviour is the Woods-Saxon potential given by

$$V(r) = \frac{-V_0}{1 + e^{\frac{r-R}{a}}} \quad (2.1)$$

where V_0 is the potential depth, R is the nuclear radius, and a is the diffuseness parameter determining the extent of the region affected by surface effects. An example calculation for this shell structure is displayed in figure 2.1. The large energy gaps and hence

predicted magic numbers for the Woods-Saxon potential are $Z, N = 2, 8, 20, 40, 58, 92$, where N is the neutron number and Z is the proton number. These values do not agree with the experimental values of $Z, N = 2, 8, 20, 28, 50, 82$ in nuclei beyond $Z, N = 20$.

In order to account for the experimental magic numbers an extra interaction must be added to the potential. An added spin-orbit coupling term is found to successfully explain the experimentally observed magic numbers [May55], splitting of levels due to this coupling term is shown in figure 2.1 on the right side. A spin orbit coupling term is added to the Woods-Saxon potential. The spin orbit term has the form

$$V_{so} = f(r)\langle\vec{l}\cdot\vec{s}\rangle, \quad (2.2)$$

where \vec{l} is the orbital angular momentum operator and \vec{s} is the spin angular momentum operator. Using the result

$$2\vec{s}\cdot\vec{l} = \vec{j}^2 - \vec{l}^2 - \vec{s}^2, \quad (2.3)$$

where \vec{j} is the total angular momentum operator, the potential becomes

$$V_{so} = \frac{1}{2}\hbar^2 f(r)[j(j+1) - l(l+1) - s(s+1)] \quad (2.4)$$

As the particles in the nucleus are spin-half nucleons, $s = \frac{1}{2}$. This spin-orbit interaction contains only terms that commute with the operators for the z -projection of the orbital angular momentum, therefore l remains a good quantum number. Each orbit can then be labelled by the total angular momentum j and the orbital angular momentum l in spectroscopic notation defined in the table below. The spin-orbit interaction acts to split each state predicted by the Woods-Saxon potential into two states of angular momentum $j = l \pm s = l \pm \frac{1}{2}$, each holding $2j + 1$ nucleons, one for each angular momentum z -projection. Parity is determined by the orbital angular momentum and given by $(-1)^l$.

Table 2.1: Spectroscopic notation for orbital angular momentum.

Orbital angular momentum	Spectroscopic notation	Parity
0	s	+
1	p	-
2	d	+
3	f	-
4	g	+
5	h	-
6	i	+
7	j	-

The minimum energy states for particles within these orbits are pairs with angular momentum summing to zero. This maximises the wavefunction overlap of the two particles with time-reversed orbits without violating the Pauli exclusion principle. The

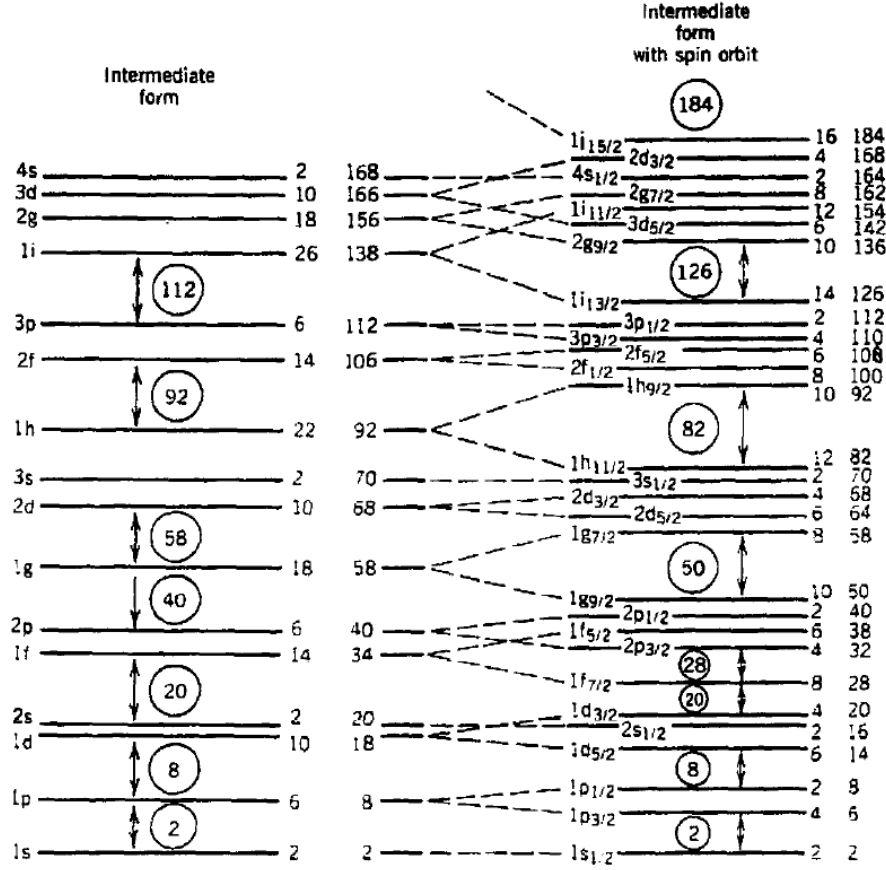


Figure 2.1: Shell model calculations of particle orbits using a Woods-Saxon potential, figure taken from Ref. [Kra88]. Splitting of levels is shown as a spin-orbit coupling term is added to the Woods-Saxon potential.

nucleon pairing effect causes the ground state in all even-even nuclei, those with even proton and neutron numbers, to be 0^+ . For spherical nuclei, this pairing effect can also be used to predict the ground state of odd mass nuclei. Separating paired nucleons costs energy of order 1 MeV and so the ground state of the nucleus can be described by the state of the single unpaired nucleon. In short, the spin and parity of the ground state is then given by the spin and parity of the orbit in which the unpaired nucleon resides.

2.2 Nilsson orbits and state mixing

In deformed (non-spherical) nuclei the spherically symmetric potential is often replaced with an axially-symmetric deformed potential called the Nilsson potential [Row10]. In

this potential l is no longer a good quantum number and mixing of spherical states with different l may occur. The new orbits in the deformed potential can be described by the principal quantum number, determining parity, and the projection of the angular momentum onto the symmetry axis Ω . The Nilsson orbits are often determined in a basis of spherical states, i.e. Nilsson orbits may be described as weighted sums of the orbits from the shell model. In the example Nilsson scheme in figure 2.2, calculated for ^{111}Cd , positive parity orbits are displayed for small deformation. Two states repelling in this plot is a sign of mixing between the states and an associated change in character typically associated with a change in the decomposition in terms of shell model states. In the case of ^{111}Cd with a small amount of deformation, the $\frac{1}{2}^+[411]$ orbit, which starts out with $s_{\frac{1}{2}}$ parentage, becomes dominated by the $d_{\frac{3}{2}}$ component. Thus, there is a change in character from predominantly $s_{\frac{1}{2}}$ to predominantly $d_{\frac{3}{2}}$ character. This also causes changes in the electromagnetic properties of the levels, for example significantly changing the transition strengths between levels and the moments of each level. In the figure below the components of the ground state wavefunction mix strongly after a small deformation $\epsilon \approx 0.05$. The wavefunction of the $\frac{1}{2}[411]$ Nilsson orbit at this point is made of the $d_{\frac{3}{2}}$ and $s_{\frac{1}{2}}$ states with about equal weight.

2.3 Collective excitations

Away from closed shell the lowest excitations in even-even nuclei occur from collective excitations. In the collective model the underlying nucleonic structure is ignored. Instead excitations occur in degrees of freedom dependent on the shape of the nucleus. In the collective models, energy and angular momentum are shared among a large number of nucleons moving coherently; this significantly increases transition strengths between states which can be used to quantify collective behaviour. Two common models for the investigation of collective motion in nuclei are the harmonic vibrator model and the rotor model.

2.3.1 The harmonic vibrator model

Excitations in the harmonic vibrator model occur as surface vibrations around a spherical unperturbed state. The instantaneous surface radius of a vibrating nucleus can be described by a time-dependant sum over spherical harmonics $Y_{\lambda\mu}$ around an average radius R_0 . The multipole order of the vibration is given by λ with the z -projection of the angular momentum from the excitation μ .

$$R_{\theta,\phi}(t) = R_0 + \sum_{\lambda \geq 1} \sum_{\mu=-\lambda}^{\lambda} a_{\lambda\mu}(t) Y_{\lambda\mu}(\theta, \phi) \quad (2.5)$$

The oscillations of interest in this thesis occur in the quadrupole degree of freedom. The quadrupole vibrations can be quantised into phonons each with angular momentum 2^+ . The first phonon excitation is therefore 2^+ . Adding a second phonon allows three

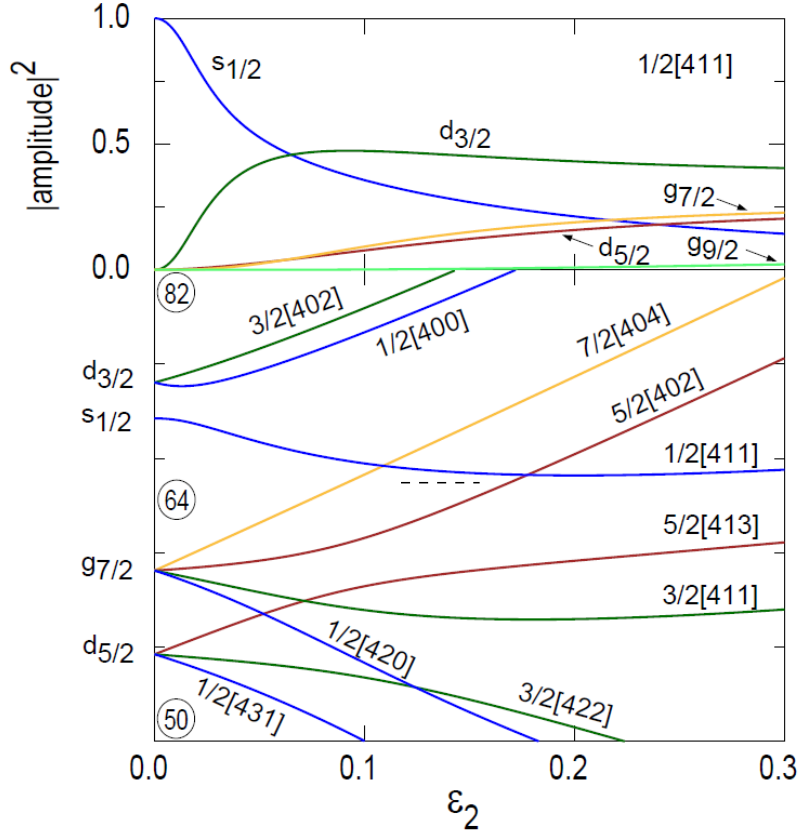


Figure 2.2: Nilsson scheme and ground state mixing for ^{111}Cd . The black dashed line indicates the approximate Fermi level of ^{111}Cd . Note that only the positive parity orbits are shown here. The negative parity $h_{11/2}$ orbit (which does not mix with positive parity states) is not shown. Figure from Ref. [Stu16].

angular momenta: 0^+ , 2^+ , and 4^+ . Assuming only quadrupole modes are excited, the Hamiltonian is given by

$$\hat{H}_{HV} = \sum_{\mu=0,\pm 1,\pm 2} \hbar\omega (b_{\mu}^{\dagger} b_{\mu} + \frac{1}{2}). \quad (2.6)$$

The operators b_{μ}^{\dagger} and b_{μ} are the creation and annihilation operators for quadrupole phonons with z -projection μ and the phonon energy is given by $\hbar\omega$. We must now consider the predictions of this model. The energies predicted by this model are given by $E_N = \hbar\omega(N + \frac{5}{2})$, where N is the phonon number of the state. As such, in this model any states with the same number of phonons should have the same energy the energies of excited states are linearly proportional to the number of phonons. That is, single phonon states have excitation energy $\hbar\omega$, 2-phonon states have twice that energy and three phonon states excite at thrice the phonon energy. Splitting of these energy

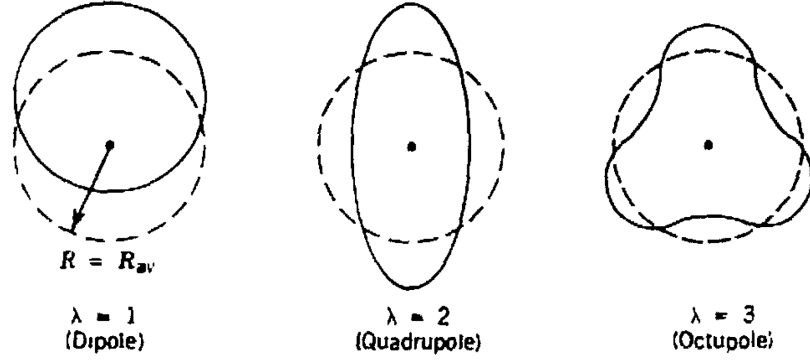


Figure 2.3: The motion of nuclear vibrations of dipole, quadrupole, and octupole order. Figure from Ref. [Kra88].

levels may occur in nuclei due to effects not considered in this model. A low lying 2^+ state with three roughly degenerate states of spin 0^+ , 2^+ , and 4^+ at about twice the 2^+ excitation energy is observed in many nuclei, particularly the even cadmium, tellurium and palladium isotopes. In figure 2.4 the lower excited states in ^{112}Cd clearly show the predicted level structure.

Predictions can also be made for the relative transition strengths with a simple $E2$ operator governing transitions between states. The operator has the assumed form

$$\mathfrak{M}(E2) = \alpha(b_\mu^\dagger + b_\mu) \quad (2.7)$$

that connects states with a difference in phonon number $\Delta N = 1$. (A term connecting states with a greater difference in phonon number can be added however it does not affect the predictions made here.) The elements of the operator connecting these states must take this form in order to maintain symmetry in excitation and de-excitation.

The strengths of transitions between levels are generally written in terms of reduced transition strengths. The general expression for a reduced transition expression depends on the square of the matrix elements.

$$B(X\lambda) = \frac{1}{2I_i + 1} \sum_{M_i} \sum_{M_f} \sum_{\mu} |\langle I_f M_f | \mathfrak{M}(X\lambda; \mu) | I_i M_i \rangle|^2 \quad (2.8)$$

where X can take the value E or M for electric or magnetic transitions, λ is the multipolarity of the transition, and I_i and I_f are the angular momenta of the initial and final states with z -projections M_i and M_f , respectively. Substituting the electric quadrupole operator of equation 2.7 into equation 2.8 and evaluating for the transitions between the first excited state and the ground state gives the result $B(E2; 2_1^+ - 0_1^+) = |\alpha|^2$. Similarly, transitions from the two phonon states to the single phonon state are found to have twice this transition strength. Experimentally, it has been shown that the re-

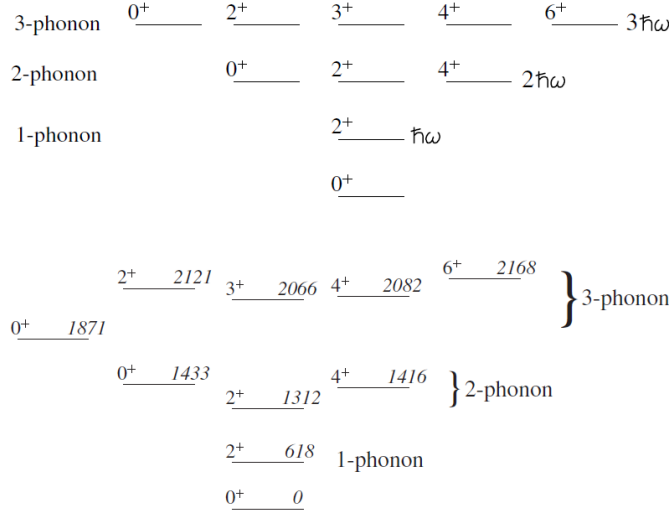


Figure 2.4: ^{112}Cd comparison with predicted harmonic oscillator structure. Good agreement is seen between the level structures from the model and experiment. Figure from Ref. [Gar10].

duced transition strengths for the transitions from the two phonon 0_2^+ and 2_2^+ states to the single phonon state 2_1^+ are significantly weaker than these predictions with $B(E2; 2_2^+ - 2_1^+) \approx 0.5 \times B(E2; 2_1^+ - 0_1^+)$ and $B(E2; 0_2^+ - 2_1^+) \approx 3 \times 10^{-4} \times B(E2; 2_1^+ - 0_1^+)$ in ^{112}Cd [Gar10], similar deviations are also seen in $^{110,114,116}\text{Cd}$. These results cast significant doubts on the validity of the harmonic vibrator model. In order to account for this behaviour it has been shown that it is necessary to add anharmonicity to the vibration and to identify the excited 0^+ state as a deformed nuclear shape due to an “intruder configuration”, i.e. a fundamentally different type of nuclear excitation. These intruder configurations are strongly excited in two-nucleon transfer reactions, which adds evidence that excited 0^+ states in the even Cd isotopes are not part of a vibrational structure. Shape coexistence in these structures has been experimentally verified with measurements of electric quadrupole moments discussed later. Though parenthetical to the experimental investigation described here, shape coexistence is an interesting phenomenon and the attribution of excited 0^+ states to shape coexistence rather than vibrational excitations forms part of the justification for investigation of ^{111}Cd [Hey83, Hey11, Woo92].

2.3.2 Rotational excitations

In deformed nuclei the simplest model for collective motion is the rotor model in which the nucleus is given a static deformation and excitations are allowed in rotational degrees

of freedom. The rotor Hamiltonian for such nuclei is given by

$$\hat{H}_{rot} = \frac{\hbar^2}{2} \left(\frac{\hat{R}_1^2}{\mathfrak{I}_1} + \frac{\hat{R}_2^2}{\mathfrak{I}_2} + \frac{\hat{R}_3^2}{\mathfrak{I}_3} \right), \quad (2.9)$$

where \mathfrak{I}_i , $i = 1, 2, 3$ are the moments of inertia in axes relative to the intrinsic statically deformed shape, and \hat{R}_i are the components of rotational angular momentum operators in each axis. In general it is necessary to consider the coupling of additional particles or excitations to a rotor core. Thus if the rotor core has an angular momentum \mathbf{R} and the intrinsic angular momentum is \mathbf{J} , with total \mathbf{I} , the rotational Hamiltonian in equation 2.9 can be rewritten using the relation

$$\mathbf{R} = \mathbf{I} - \mathbf{J}, \quad (2.10)$$

thus obtaining

$$\hat{H}_{rot} = \sum_i \frac{\hbar^2}{2} \frac{\hat{I}_i^2}{\mathfrak{I}_i} - \sum_i \frac{\hbar^2}{2} \frac{\hat{I}_i \hat{J}_i}{\mathfrak{I}_i} + \sum_i \frac{\hbar^2}{2} \frac{\hat{J}_i^2}{\mathfrak{I}_i}. \quad (2.11)$$

The third term in this expression is the centrifugal term often ignored in calculations. The coupling term between the intrinsic and total angular momentum in this equation is the Coriolis term and can be ignored for even-even nuclei with the assumption that the frequency of rotational excitations is much lower than for intrinsic excitations; this is known as the adiabatic approximation. (A full particle-rotor calculation includes the Coriolis term, which mixes states with different K .) The energy levels for this Hamiltonian cannot generally be analytically solved, however they can be determined by diagonalisation of the Hamiltonian. Observationally, only the even spin states are seen in even-even nuclei suggesting that the shape of the nucleus is symmetric across a plane perpendicular to an axis of symmetry [Eis87, Kra88, Row70, Row10]. Thus setting two components of angular momentum equal to each other we arrive at the symmetric top model, the most common model for rotational nuclei.

The energy of excitations in this model can be solved for and are given by

$$E_{KI} = \frac{\hbar^2}{2} \left[\frac{I(I+1)}{\mathfrak{I}} + \left(\frac{1}{\mathfrak{I}_3} - \frac{1}{\mathfrak{I}} \right) K^2 \right]. \quad (2.12)$$

Here, K is the projection of the total angular momentum on the symmetry axis, and \mathfrak{I}_3 is the moment of inertia for this axis. The ground states in even-even nuclei are therefore expected to have rotational bands with energies $E_I = \frac{\hbar^2}{2} \frac{I(I+1)}{\mathfrak{I}}$. These levels are well documented in mid-shell deformed nuclei, however higher spin states in this ground band begin to move closer together, suggesting centrifugal stretching of the nucleus which is ignored in the adiabatic approximation.

The shape of nuclei in the symmetric rotor model can be parameterised as

$$R_{\theta,\phi} = R_{av} (1 + \beta Y_{20}(\theta, \phi)) \quad (2.13)$$

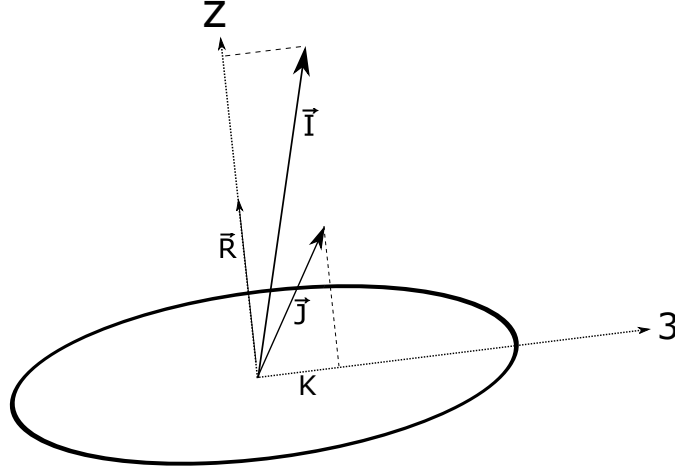


Figure 2.5: A deformed rotating nucleus, K is defined as the projection of the intrinsic spin onto the axis of symmetry.

where R_{av} is the average nuclear radius, and β is a nuclear deformation parameter defined by

$$\beta = \frac{4}{3} \sqrt{\frac{\pi}{5}} \frac{\Delta R}{R_{av}}, \quad (2.14)$$

with ΔR the difference between semi-major and semi-minor axes [Kra88]. The two possible shapes with the required symmetries are then prolate deformed nuclei with $\beta > 0$ and oblate deformed nuclei with $\beta < 0$. Experimentally, it is shown that prolate deformation is preferred in nuclei. Depending on the parametrization of the deformed potential the deformation parameter might be denoted β or ϵ . As a very rough approximation $\beta \approx \epsilon$. It has been previously shown that the low lying excited states in even mass Cd nuclei have intrinsic electric quadrupole moments consistent with a deformed nucleus with a deformation parameter $\epsilon \approx 0.1$. This corresponds to slight prolate deformation of the nucleus.

2.3.3 The particle-vibrator model

Spherical odd- A nuclei (nuclei with an odd number of nucleons) are often modelled by coupling the single-particle orbit of the odd nucleon to the vibrational excitation of the core of the neighbouring even-even nucleus. The 2^+ phonon can couple with the j angular momentum of the core to create states with I from $|j - 2|$ to $j + 2$.

In the weak-coupling model, interaction terms in the Hamiltonian are ignored. Basis states for the coupled system can then be expanded in terms of the basis states for the single particle and the quadrupole vibration using Clebsch-Gordan coefficients as described in appendix A [Eis87]. The states are thus

$$|j; NR; IM\rangle = \sum_{m_1 m_2} \langle IjJ | m_1 m_2 M \rangle |NIM\rangle |jm_2\rangle \quad (2.15)$$

where N is the phonon number, R is the angular momentum of the surface vibration, j is the single particle angular momentum with energy E_j , m_1 and m_2 are the z -projection of the core angular momentum and the single particle angular momentum respectively, with I and M the total angular momentum and its z -projection. The energy levels in this model are then given by

$$(H_c + H_p) |j; NR; IM\rangle = (N\hbar\omega + E_j) |j; NR; IM\rangle \quad (2.16)$$

where $\hbar\omega$ is the phonon energy and E_j is the energy of the single particle orbit. This is a useful initial model for studying basic properties of odd- A nuclei. However, in order to study observed structure in these nuclei a more sophisticated model is required.

2.3.4 Theoretical particle-vibration calculations

The calculation of states in this thesis proceeds via the particle-vibration model, sometimes in older literature referred to as the intermediate coupling model in the unified nuclear model [Cho67]. In the “unified model” features of the shell model and the collective model are combined for odd mass nuclei. The odd nucleon is coupled to the even-even collective core as in the weak-coupling model with the initial basis states taken to be those in the weak-coupling model. An extra interaction term is then added which couples these two systems and mixes states;

$$H_{int} = -\sqrt{\frac{1}{5}}\pi \xi \hbar\omega \sum_{\mu} (b_{\mu} + (-)^{\mu} b_{-\mu}^+) Y_{2\mu}(\theta\phi), \quad (2.17)$$

where b_{μ}^+ and b_{μ} are the creation and annihilation operators for core phonons with z -projection μ , the spherical harmonic $Y_{2\mu}$ has the angular coordinates of the unpaired nucleon. The coupling parameter ξ is defined by

$$\xi = k \sqrt{\frac{5}{2}} \hbar\omega C \quad (2.18)$$

where k is the average coupling constant, and C is the surface stiffness parameter. Diagonalising the new Hamiltonian

$$H = H_c + H_p + H_{int} \quad (2.19)$$

allows the energy levels for these states to be calculated. Once the new eigenstates are found other electromagnetic properties can be found such as the $B(E2)$ and $B(M1)$ values, and the magnetic dipole moment, as discussed later in Section 2.4.2.

2.3.5 The particle-rotor model

In deformed, odd- A nuclei we expect coupling between the single particle orbit and the rotational motion. The expression for the rotor Hamiltonian is again that in equation

2.11. The system is then described by the superposition of the intrinsic motion of the particle and the rotor. The intrinsic motion of the odd nucleon can be taken to be that of the corresponding Nilsson orbit. Often the strong coupling limit, that is no Coriolis or centrifugal interactions between the single particle orbit and the rotational motion, is applied.

Rotational bands built on the single particle states increase in angular momentum by integer values [Boh75]. An example level scheme for rotational excitations on single particle states is shown in figure 2.6. In this case there are bands built on Nilsson orbits with $K^\pi = \frac{3}{2}^-$ and $K^\pi = \frac{9}{2}^+$.

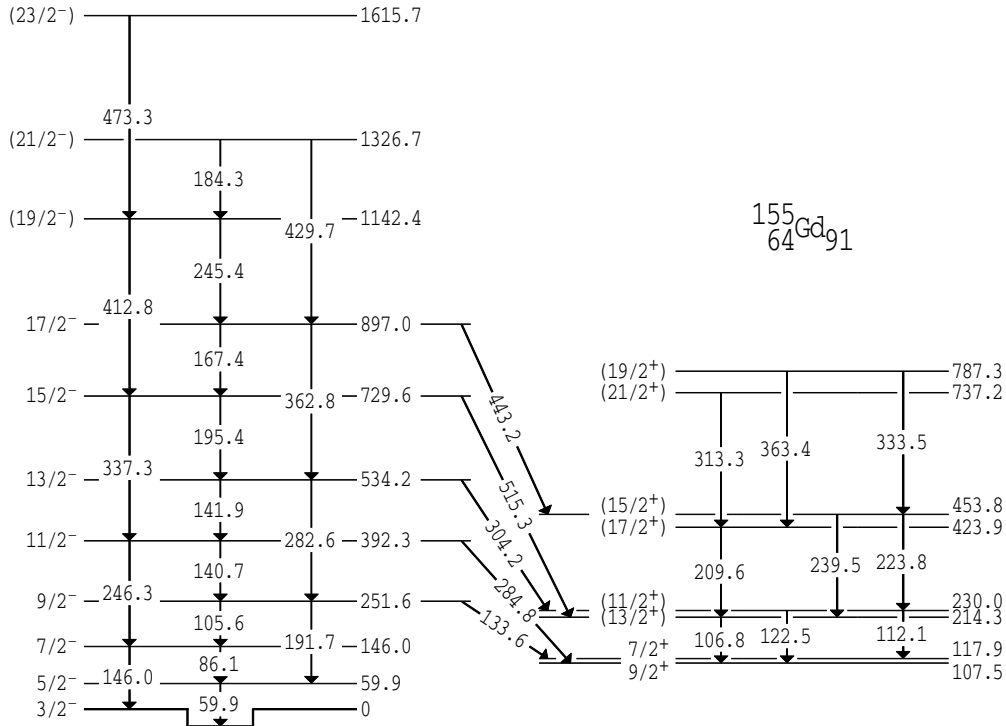


Figure 2.6: The experimental level scheme of ^{155}Gd , an odd mass rotational nucleus. Figure from Ref. [Stu98].

2.4 Electromagnetic moments of nuclei

2.4.1 Electric quadrupole moments

A set of important quantities when describing nuclei are the electric and magnetic moments. In spherical nuclei the symmetry causes zero electric quadrupole moments; in harmonic vibrators these symmetries are maintained and the electric quadrupole moment

remains zero. Classically, the electric quadrupole moment is given by

$$Q_0 = \int \rho(2z^2 - x^2 - y^2)dV, \quad (2.20)$$

where ρ is the charge density and the integral is over the volume of the object. This moment is a direct measure of the asymmetry of charge distribution in the structure. Quantum mechanically the electric quadrupole moment in deformed nuclei is dependent on the spin, its projection on the symmetry axis and the intrinsic quadrupole moment which is constant for a given rotor band [Boh75].

$$Q(\alpha KI) = \frac{3K^2 - I(I+1)}{(I+1)(2I+3)} e\bar{Q}_0(\alpha K) \quad (2.21)$$

where α defines the band and $\bar{Q}_0(\alpha K)$ is the intrinsic quadrupole moment.

2.4.2 Magnetic moments and g factors

The magnetic moment of a nucleus is a measure of the distribution of angular momentum amongst its charges. Additionally, the nucleons also have intrinsic magnetic moments associated with their intrinsic spin. The experimental magnetic moment of a proton is $\mu_p = 2.794\mu_N$ and the magnetic moment of the neutron is $\mu_n = -1.913\mu_N$ where μ_N is the nuclear magneton [May55].

Magnetic moments of a nucleus are generally directly related to nuclear gyromagnetic ratios, known as g factors. The magnetic moment is related to the g factor by

$$\mu = gI\mu_N \quad (2.22)$$

where I is the total spin of the system. Therefore, the spin g factors for free nucleons are $g_s = 5.59$ for protons and $g_s = -3.83$ for neutrons. As a first approximation these are assumed to remain the same within the nucleus while a further orbital component is coupled, with $g_l = 1$ for protons and $g_l = 0$ for neutrons. Experimentally, it is demonstrated that better agreement with measured moments is found by quenching the spin g factor to 0.7 of the free value. The magnetic dipole operator is given by

$$\hat{\mu} = \sum_i (g_l^i \hat{\mathbf{l}}_i + g_s^i \hat{\mathbf{s}}_i) \quad (2.23)$$

where $\hat{\mathbf{l}}$ is the orbital angular momentum operator, and $\hat{\mathbf{s}}$ is the spin angular momentum operator. The calculation of a magnetic moment of a nucleus proceeds by taking the expectation value, with the requirement that the state has maximum z -projection

$$\langle \mu \rangle = \langle JM = J | \sum_i g_l^i \hat{\mathbf{l}}_i + g_s^i \hat{\mathbf{s}}_i | JM = J \rangle = \langle JM = J | \sum_i g_l^i \hat{\mathbf{j}}_i + (g_s^i - g_l^i) \hat{\mathbf{s}}_i | JM = J \rangle. \quad (2.24)$$

where $\hat{\mathbf{j}}$ is the total angular momentum operator. In the case of an odd-mass nucleus with

a single unpaired nucleon the approximation can be made that the magnetic moment is determined entirely by the unpaired nucleon [Kra88]. Only the z -component with spin in the $\hat{\mathbf{J}}$ direction is being taken here and so $s_z = \frac{|\hat{\mathbf{S}} \cdot \hat{\mathbf{J}}| \hat{J}}{|\hat{\mathbf{J}}|^2}$ and

$$\langle s_z \rangle = \frac{j}{2j(j+1)}(j(j+1) - l(l+1) + s(s+1)). \quad (2.25)$$

The equation therefore simplifies to
for $j = l + \frac{1}{2}$

$$\langle \mu \rangle = \mu_N(g_l(j - \frac{1}{2}) + \frac{g_s}{2}) \quad (2.26a)$$

for $j = l - \frac{1}{2}$

$$\langle \mu \rangle = \mu_N(g_l \frac{j(j + \frac{3}{2})}{j+1} + \frac{g_s}{2} \frac{1}{j+1}). \quad (2.26b)$$

These predicted values are called the Schmidt limits, with measured values of g -factors generally falling within these lines.

In the rotor model the g -factors are split into core and rotor components. The magnetic dipole operator in this case is

$$\hat{\mu} = g_R \hat{\mathbf{I}} + \sum_i ((g_l^i - g_R) \hat{\mathbf{I}}_i + (g_s^i - g_R) \hat{\mathbf{s}}_i) \quad (2.27)$$

where g_R is the gyromagnetic ratio for the rotor and $\hat{\mathbf{I}}$ is the angular momentum operator for the core. [Boh75] Introducing the intrinsic g factor, g_K and the magnetic decoupling parameter b , which is constant for a given rotor band, the g factor in the rotor model with an intrinsic spin of $\frac{1}{2}$ may be written as

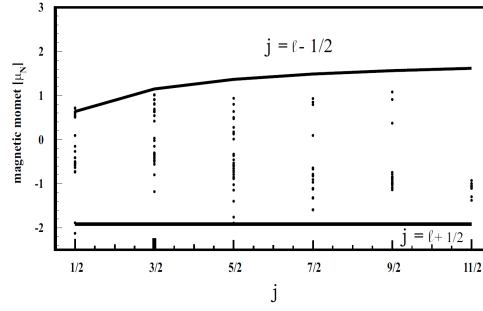
$$g = g_R + \frac{(g_K - g_R)}{4I(I+1)} [1 + (2I+1)(-1)^{I+\frac{1}{2}} b]. \quad (2.28)$$

In the particle-rotor model the g factor for the core is that of the rotating spheroid. Its g factor given by the ratio of the partial angular momentum of the protons to that of both the protons and neutrons. Assuming equal angular momentum carried by both groups the hydrodynamic value is obtained, $g_R = \frac{Z}{A}$ [Cas90]. Deviations from this value are generally negative, indicating that more angular momentum is held in the neutrons than protons.

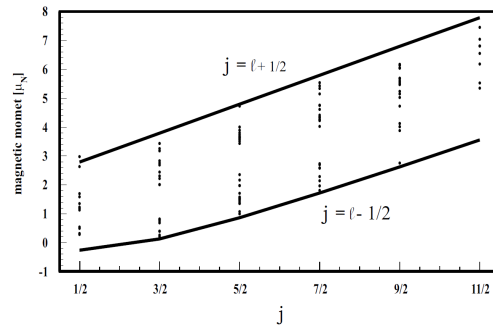
For spherical nuclei with an odd nucleon we can start by assuming weak coupling between the odd nucleon and the core. The Landé addition formula calculates the expected g factor for the combined system:

$$g = \frac{1}{2}(g_c + g_j) + \frac{1}{2}(g_c - g_j) \frac{J_c(J_c + 1) - j(j + 1)}{I(I + 1)}. \quad (2.29)$$

In the case where this relates to coupling a vibration and a single particle, g_c is the



(a)



(b)

Figure 2.7: Schmidt lines for magnetic moments in a) odd-neutron nuclei, b) odd-proton nuclei, with experimental data points. Figure taken from Ref. [Geo01].

core g factor, g_j is the g factor for the single particle, and J_c and j are the angular momentum of the core and the single particle, respectively. It may be shown in the limit of zero deformation in the particle rotor model the expression in equation 2.28 reduces to the weak-coupling expression for the special case where $j = K = \frac{1}{2}$, as applies in ^{111}Cd [Stu16].

Nuclear spectroscopy

3.1 Transitions

Transitions between states in a nucleus can occur through several processes, the strongest of which is usually gamma-ray emission. The extra energy and angular momentum of the excited nucleus is carried by a photon and parity is conserved. The gamma-ray can be of either electric or magnetic type. These transitions are labelled as $X\lambda$ transitions where X is E or M for electric or magnetic type decays, respectively, and λ is the angular momentum of the photon. The number λ also defines the multipolarity and angular distribution of gamma-rays with $\lambda=1$ a dipole transition, $\lambda = 2$ a quadrupole transition, etc. The allowed decays between two states of angular momentum J_i and J_f are parity conserving decays of angular momentum $|J_i - J_f| \leq \lambda \leq J_i + J_f$. As shown in the table below the transitions alternate between parity conserving and parity changing transitions as multipolarity increases and the type of transition changes. The parity is given by $\pi = (-1)^\lambda$ for electric transitions and $\pi = (-1)^{\lambda+1}$ for magnetic transitions.

Table 3.1: Parity of transitions between nuclear states.

	1	2	3	4	5
M	+	-	+	-	+
E	-	+	-	+	-

The strength of transitions also decreases with increasing multipolarity, with electric transitions stronger in general than magnetic transitions. Reduced transition rates are defined by

$$B(X\lambda; I_i \rightarrow I_f) = \frac{\lambda[(2\lambda + 1)!!]^2 \hbar}{8\pi(\lambda + 1)} \left(\frac{\hbar c}{E_\gamma}\right)^{2\lambda+1} P_\gamma(X\lambda; I_i \rightarrow I_f), \quad (3.1)$$

where $P_\gamma(X\lambda; I_i \rightarrow I_f)$ is the partial decay probability [Ald75]. In the case of a pure multipolarity and a single transition out of a state, the decay probability is the inverse of the mean life, $\frac{1}{\tau}$. The general case is more complicated when multiple gamma-ray branches are possible or mixed transitions occur. It is more instructive, however, to evaluate the

constants for each transition and consider the relative size of each contribution.

Table 3.2: Numerically evaluated formulae for reduced transition strengths with energy in MeV and transition probabilities P_γ in s^{-1} .

λ (\hbar)	$B(E\lambda)$ ($e^2\text{fm}^{2\lambda}$)	$B(M\lambda)$ ($e\hbar/2M_p \text{ fm}^{2(\lambda-1)}$)
1	$6.288 \times 10^{-16} E_\gamma^{-3} P_\gamma(E1)$	$5.687 \times 10^{-14} E_\gamma^{-3} P_\gamma(M1)$
2	$8.161 \times 10^{-10} E_\gamma^{-5} P_\gamma(E2)$	$7.381 \times 10^{-8} E_\gamma^{-5} P_\gamma(M2)$
3	$1.752 \times 10^{-3} E_\gamma^{-7} P_\gamma(E3)$	$1.584 \times 10^{-1} E_\gamma^{-7} P_\gamma(M3)$

Transition strengths are often given in Weisskopf units $\frac{B(X\lambda)}{B_W(X\lambda)}$, multiples of the transition strength for a single particle transition as given by a simple Weisskopf estimate. The Weisskopf estimates are given in table 3.3. Evaluating the strength of the transition in Weisskopf units clearly shows whether a transition is single particle in nature as indicated by a strength around 1 W.u., or collective in which case the strength is many W.u. [Ald75].

Table 3.3: Single-particle Weisskopf estimates of transition strengths, numerically evaluated, where A is the mass number of the nucleus.

λ (\hbar)	$B_W(E\lambda)(e^2\text{fm}^{2\lambda})$	$B_W(M\lambda)(e\hbar/2M_p \text{ fm}^{2(\lambda-1)})$
1	$0.06446A^{\frac{2}{3}}$	1.7905
2	$0.05940A^{\frac{4}{3}}$	$1.6501A^{\frac{2}{3}}$
3	$0.05940A^2$	$1.6501A^{\frac{4}{3}}$

When comparing experimental results to theoretical results, generally reduced transition strengths, (e.g. $B(E2)$ or $B(M1)$ values), are used. Comparing transition strengths rather than level lifetimes allows comparisons of the nuclear transition strength with the strong transition-energy dependant factor removed. Theoretical calculations of transition strengths proceed as in equation 2.8.

3.2 Isomeric states and decay curves

Transitions with low energy or high multipolarity are hindered. If other decay paths are not possible this can lead to isomeric states, i.e. states with long lifetimes. If the lifetime of the state is long enough for the detector to resolve, it is possible to form a decay curve showing the exponential decay of the state. The time resolution of the High Purity Germanium (HPGe) detectors used in this experiment is on the order of 10 ns allowing the decay of longer lived states with lifetimes of several tens of ns to be observed. The first excited state in ^{111}Cd has a half-life of 84.5(4) ns [Bla09]. In this

work a comparison decay curve was measured in order to test that the timing electronics were functioning correctly. The rate of decay of excited states in nuclei is governed by the equation

$$N(t) = N(0)e^{-\frac{t}{\tau}} \quad (3.2)$$

where $N(t)$ is the number of nuclei present, t is the time and τ is the mean life. Fitting a decay curve with a function of this form allows the mean life of the state to be determined. As noted above the reduced transition rate, (e.g. $B(E2)$), can be determined from the measured lifetimes. Figure 3.1 displays a previously measured decay curve for the 245 keV state in ^{111}Cd .

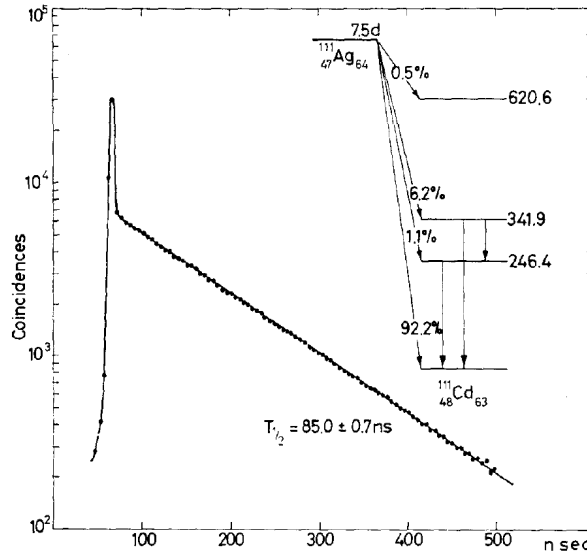


Figure 3.1: A previously measured decay curve for the 245 keV state. Figure from [Mcd68]

3.3 Example: The decay and g factor of the $\frac{5}{2}^+$ state in ^{111}Cd

Many of the concepts introduced above may be illustrated by the first-excited state of ^{111}Cd . The $I^\pi = \frac{5}{2}^+$ state at 245 keV in ^{111}Cd has a previously measured g factor of $g = -0.306$ [Bla09]. The Schmidt value for a $d_{5/2}$ neutron is $g = -0.765$. Standard quenching of the spin-orbit g factor takes the value to between 0.6 and 0.7 of the Schmidt value. This brings the expected g factor into better agreement with the experimental value. Thus, the 245 keV state can be attributed to the odd neutron occupying the $\nu d_{5/2}$ orbit ($l = 2, j = \frac{5}{2}$), at least as the dominant configuration in the wavefunction.

Turning to the isomeric $E2$ decay of the $\frac{5}{2}^+$ state to the ground state, it is found that

the transition strength is $B(E2) = 0.22$ W.u., about $\frac{1}{5}$ of the single particle Weisskopf estimate. As the $\frac{5}{2}^+$ is the first excited state in the nucleus, and is at low energy, a hindered decay is expected if this state corresponds to a single-particle excitation of the odd neutron from a $\nu s_{\frac{1}{2}}$ ground state to a $\nu d_{\frac{5}{2}}$ orbit.

3.4 Angular distributions and correlations

The theory governing the angular distribution of gamma decays in a nucleus outlined here follows that of Morinaga and Yamazaki [Mor76], and proceeds simply from the Poynting vector, which defines the linear momentum density.

$$\mathbf{P} = \frac{c}{4\pi} \mathbf{E} \times \mathbf{H} \quad (3.3)$$

The magnitude of this vector then gives the intensity of radiation in that direction. The electric or magnetic field for electromagnetic radiation can be described by sums of spherical harmonics $Y_{l\mu-m}$. The multipolarity of the transition λ is the total angular momentum of the emitted radiation, l is the orbital angular momentum for the transition and takes values $\lambda+1$, λ , and $\lambda-1$ for the spin one photon, and μ is the z -axis component for the subprocess of the given transition. The expression for this state is then

$$X_{\lambda\mu} = \sum_m \langle l \mu - m \ 1 \ m | \lambda \mu \rangle Y_{l\mu-m} \xi_m, \quad (3.4)$$

where the ξ_m are the spherical unit vectors. The parity of this expression is determined by λ as determined by the spherical harmonics. The magnitude of the electric and magnetic field are each equal to the magnitude of the expression in equation 3.4, hence the angular distribution of decay radiation becomes

$$\begin{aligned} |\mathbf{P}|^2 &= Z_{\lambda\mu}(\theta, \phi) = |X_{\lambda\mu}|^2 = \left| \sum_m \langle l \mu - m \ 1 \ m | \lambda \mu \rangle Y_{l\mu-m} \xi_m \right|^2 \\ &= \frac{(-1)^{\mu-1}}{4\pi} \sum_k \langle \lambda 1 \lambda - 1 | k 0 \rangle \langle \lambda \mu - m \ 1 m | \lambda \mu \rangle P_k(\cos \theta) \end{aligned} \quad (3.5)$$

The results for $\lambda = 1$ and $\lambda = 2$ subprocesses are displayed in figure 3.2.

Decays from oriented states form distributions from classical probability distributions of the magnetic substates. To model this effect the population parameter $P(m)$ is introduced which describes the relative occupation of the m -substates. In Coulomb excitation reactions the excited state is “aligned”, i.e. $P(m) = P(-m)$. Alignment and polarization together define the “orientation”, the population of each magnetic substate. Excitations in Coulomb excitation reactions occur in a defined direction, populating magnetic substates with this orientation, however this effect is reduced when exciting from high spin states that can couple in further ways to the excitation angular momentum [Lam90].

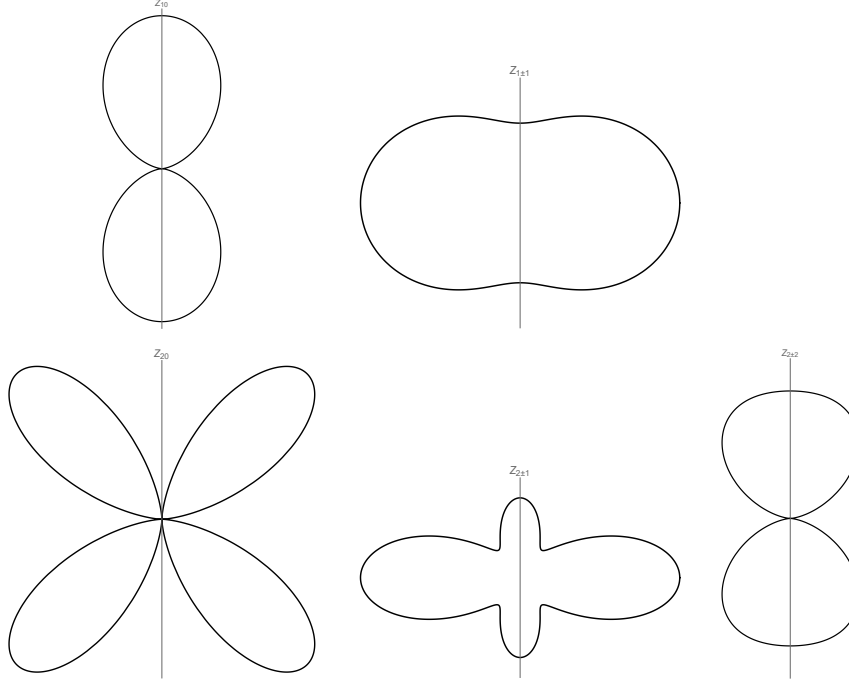


Figure 3.2: Angular distributions for gamma-decay subprocesses $Z_{\lambda\mu}$, where λ is the multipolarity and μ is the change in the z -projection between states.

The final spatial distribution of gamma decays is then the sum of the functions for a transition from a defined magnetic substate $Z_{\lambda\mu}(\theta\phi)$ multiplied by the population of that substate and the transition strength for that process. The Wigner-Eckart theorem can be applied to separate the transition strengths into two components, a Clebsch-Gordan coefficient and a geometric quantity independent of the populated magnetic substate.

$$\langle j_f m_f | \lambda \mu | j_i m_i \rangle = \langle j_i m_i \lambda \mu | j_f m_f \rangle \langle j_f || \lambda || j_i \rangle \quad (3.6)$$

The geometric factor is the same for all subprocesses and is ignored. The angular distribution for this transition is thus given by

$$W(\theta) = \sum_{m_i, \mu} |\langle j_i m_i \lambda \mu | j_f m_f \rangle|^2 P(m_i) Z_{\lambda\mu}(\theta, \phi) \quad (3.7)$$

This distribution is further simplified with the introduction of the statistical tensor and Racah W-coefficients (see Appendix B). The statistical tensor is defined, using the conventions of Morinaga and Yamazaki (Ref. [Mor76]), as

$$\rho_k(j) = \sqrt{2j+1} \sum_m (-1)^{j-m} \langle j m j - m | k 0 \rangle P(m) \quad (3.8)$$

and the F coefficient is defined as

$$F_k(j_f \lambda j_i) = (-1)^{1+j_i-j_f} \sqrt{2j_i+1} (2\lambda+1) \langle \lambda 1 \lambda -1 | k 0 \rangle W(j_i j_i \lambda \lambda; k j_f) \quad (3.9)$$

Therefore

$$W(\theta) = \sum_k \rho_k(j_i) F_k(j_i \lambda j_f) P_k(\cos \theta) \quad (3.10)$$

Here ρ_k contains the information on the initial distribution of magnetic substates in the nucleus and F_k contains the information about the multipolarity of the transition and the final state information. The angular dependence in this expression is given by the sum over the Legendre polynomials $P_k(\cos \theta)$; these replace the spherical harmonics as the distribution is usually symmetric in ϕ , i.e. around the beam axis. Example angular distributions for various multipolarities are shown in figure 3.3.

The non-zero elements for dipole $\lambda = 1$ transitions are the $k = 0, 2$ components and for quadrupole $\lambda = 2$ the non-zero elements are the $k = 0, 2, 4$ components. Transitions are often written in terms of A_k coefficients as in the equation below.

$$W(\theta) = A_0 \left(1 + \sum_{k=2,4} A_k P_k(\cos \theta) \right) \quad (3.11)$$

Angular correlations are the angular dependant decay probabilities for gamma-radiation with respect to a coincident radiation. In this thesis Coulomb excitation is taken as the initial transition, defining the direction of the transition by detection of backscattered particles. In this way the multipolarity of the transition can be determined by measuring the proportion of gamma decays at a range of angles and thus determining the shape of the angular correlation.

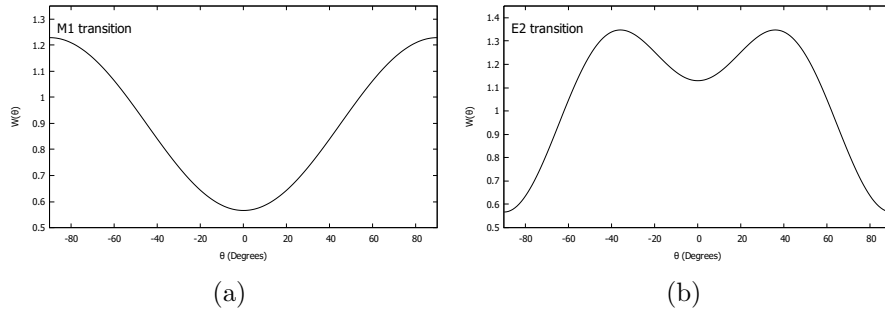


Figure 3.3: a) Example $M1$ transition angular distribution. b) Example $E2$ transition angular distribution. These shapes are relatively insensitive to the initial spin value. θ is the angle to the beam axis.

3.5 Mixed transitions

For each transition the allowed angular momenta carried by the electromagnetic field range from $|J_i - J_f| \leq \lambda \leq J_i + J_f$. However, allowed multipolarities can mix coherently allowing for a continuous range of angular distributions. The most common type of electromagnetic transition between low excitation states of collective nuclei is $E2$ - a consequence of quadrupole collectivity. The most common type of mixed multipolarity is then $E2/M1$ mixing. Such mixing is likely when $|J_i - J_f| \leq 1$ while $J_i + J_f \geq 2$. The shape of the angular distribution is then determined by the proportion of the transition from each multipolarity. The mixing ratio is defined as

$$\delta = \frac{\langle j_f | (\lambda_1) | j_i \rangle}{\langle j_f | (\lambda_2) | j_i \rangle}. \quad (3.12)$$

This is the ratio of the energy independent transition amplitudes for each multipolarity. The mixing ratio for $E2/M1$ transitions is generally given as $\delta(E2/M1)$, i.e. $\lambda_1 = 2, \lambda_2 = 1$. The angular distribution is then given by a similar expression to single multipolarity transitions. In mixed transitions a new definition of the F coefficient is formed

$$F_k(j_f \lambda_1 \lambda_2 j_f) = (-1)^{1+j_i-j_f} \sqrt{(2j_i+1)(2\lambda_1+1)(2\lambda_2+1)} \langle \lambda_1 1 \lambda_2 -1 | k 0 \rangle \times W(j_i j_i \lambda_1 \lambda_2; k j_f). \quad (3.13)$$

The angular distribution is then defined as

$$W(\theta) = \sum_k A_k(j_i \lambda_1 \lambda_2 j_f) P_k(\cos \theta) \quad (3.14)$$

where

$$A_k(j_i \lambda_1 \lambda_2 j_f) = \rho_k(j_i) \frac{1}{1 + \delta^2} [F_k(j_f \lambda_1 \lambda_1 j_i) + 2\delta F_k(j_f \lambda_1 \lambda_2 j_i) + \delta^2 F_k(j_f \lambda_2 \lambda_2 j_i)]. \quad (3.15)$$

3.6 Magnetic perturbation of angular correlations

When a nucleus with a dipole moment is placed in a magnetic field it precesses around the magnetic field at the Larmor frequency defined by

$$\omega_L = -g \frac{\mu_N}{\hbar} B, \quad (3.16)$$

where g is the g factor of the state and B is the magnetic field. As the nucleus precesses at this frequency so does the angular distribution, if this precession is large enough it can be measured and used to infer the g factor. The modified expression for the angular

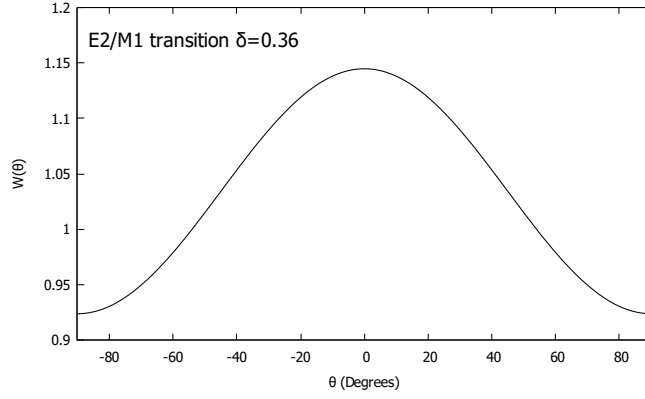


Figure 3.4: Example angular distribution for a mixed $E2/M1$ transition. δ is taken to be 0.36 as is the case for the $\frac{3}{2}^+ \rightarrow \frac{1}{2}^+$ transition in ^{111}Cd .

distribution will then become

$$W(\theta) = \sum_k \rho_k(j_i) F_k(j_i \lambda j_f) P_k(\cos \theta - \omega_L t). \quad (3.17)$$

For longer lifetime transitions it is possible to observe this oscillation in the angular distribution as a function of time, however, for the measurements in this work the shorter lifetimes ensure that only part of an oscillation occurs. If the nucleus precesses for a specified short time, the deviation from the unperturbed angle is then written as

$$\Delta\theta = \omega_L t. \quad (3.18)$$

3.7 Comparing transition strengths in the weak-coupling and particle-rotor models

In ^{111}Cd the first excited $\frac{3}{2}^+$ state and second excited $\frac{5}{2}^+$ state have large $B(E2)$ values suggesting collectivity [Koi67]. In this section we look to predict the ratio of $B(E2)$ values for the first $\frac{3}{2}^+ \rightarrow \frac{1}{2}^+$ and $\frac{5}{2}^+ \rightarrow \frac{1}{2}^+$ transitions from the first collective excitations on a $\frac{1}{2}^+$ ground state in both the particle-rotor and weak-coupling particle-vibration model.

3.7.1 Weak-coupling model

The expression for the reduced transition strength of a $B(E2)$ operator in the weak-coupling model is

$$B(E2; I_i \rightarrow I_f) = \frac{|\langle I_f || \mathfrak{M}(E2) || I_i \rangle|^2}{2I_i + 1}, \quad (3.19)$$

where I_f is the final spin state, I_i is the initial spin state and $\mathfrak{M}(E2)$ is the electric

quadrupole operator. Separating the operator into core and single particle sections

$$\mathfrak{M}(E2) = \mathfrak{M}_c(E2) + \mathfrak{M}_p(E2) \quad (3.20)$$

the reduced matrix element may be expressed as

$$\begin{aligned} \langle J'_c j I_f || \mathfrak{M}_c(E2) + \mathfrak{M}_p(E2) || J_c j I_i \rangle &= (-1)^{J'_c + j + I_f} [(2I_f + 1)(2I_i + 1)]^{\frac{1}{2}} \\ &\times \left[\langle J'_c || \mathfrak{M}_c(E2) || J_c \rangle \begin{Bmatrix} J'_c & I_f & j \\ I_i & J_c & k \end{Bmatrix} + (-1)^{I_i - I_f} \langle j || \mathfrak{M}_p(E2) || j \rangle \begin{Bmatrix} j & I_f & J'_c \\ I_i & j & k \end{Bmatrix} \delta_{J_c J'_c} \right], \end{aligned} \quad (3.21)$$

where j is the angular momentum of the odd particle, J_c and J'_c are the initial and final angular momentum of the core, and I_i and I_f are the total angular momentum for the initial and final states [Sha61]. The relation between the Wigner 6j and Racah symbols is given in appendix B. If the $\frac{3}{2}^+$ and $\frac{5}{2}^+$ states in ^{111}Cd are the core excitation doublet from the $\frac{1}{2}^+$ ground state then $j = \frac{1}{2}$, $J_c = 2$, $J'_c = 0$, and $I_f = \frac{1}{2}$ in each of the transitions to the ground state. The value that changes between these two transitions is then I_i . In either case the reduced matrix element is

$$\left\langle 0 \frac{1}{2} \frac{1}{2} \right| \left| \mathfrak{M}_c(E2) + \mathfrak{M}_p(E2) \right| \left| 2 \frac{1}{2} I_i \right\rangle = (-1)[2(2I_i + 1)]^{\frac{1}{2}} \langle 0 || \mathfrak{M}_c(E2) || 2 \rangle \begin{Bmatrix} 0 & \frac{1}{2} & \frac{1}{2} \\ I_i & 2 & 2 \end{Bmatrix}. \quad (3.22)$$

For the $\frac{5}{2}^+ \rightarrow \frac{1}{2}$ transition

$$\begin{aligned} \left\langle 0 \frac{1}{2} \frac{1}{2} \right| \left| \mathfrak{M}_c(E2) + \mathfrak{M}_p(E2) \right| \left| 2 \frac{1}{2} \frac{5}{2} \right\rangle &= (-1)12^{\frac{1}{2}} \langle 0 || \mathfrak{M}_c(E2) || 2 \rangle \begin{Bmatrix} 0 & \frac{1}{2} & \frac{1}{2} \\ \frac{5}{2} & 2 & 2 \end{Bmatrix} \\ &= -\sqrt{\frac{6}{5}} \langle 0 || \mathfrak{M}_c(E2) || 2 \rangle \end{aligned} \quad (3.23)$$

while for the $\frac{3}{2}^+ \rightarrow \frac{1}{2}$ transition

$$\begin{aligned} \left\langle 0 \frac{1}{2} \frac{1}{2} \right| \left| \mathfrak{M}_c(E2) + \mathfrak{M}_p(E2) \right| \left| 2 \frac{1}{2} \frac{3}{2} \right\rangle &= (-1)8^{\frac{1}{2}} \langle 0 || \mathfrak{M}_c(E2) || 2 \rangle \begin{Bmatrix} 0 & \frac{1}{2} & \frac{1}{2} \\ \frac{3}{2} & 2 & 2 \end{Bmatrix} \\ &= \sqrt{\frac{4}{5}} \langle 0 || \mathfrak{M}_c(E2) || 2 \rangle \end{aligned} \quad (3.24)$$

Substituting these results into equation 3.19 we find

$$\frac{B(E2; \frac{5}{2} \rightarrow \frac{1}{2})}{B(E2; \frac{3}{2} \rightarrow \frac{1}{2})} = 1 \quad (3.25)$$

Thus the $B(E2) \downarrow$ strengths should be equal for the doublet in this model.

3.7.2 Particle-rotor model

In the particle-rotor model the $B(E2)$ strength for transitions within a rotational band may be expressed in terms of the intrinsic quadrupole moment Q_0 , the initial and final angular momenta I_i and I_f , and K , the intrinsic spin of the nucleus [Ald75].

$$B(E2; I_i \rightarrow I_f) = \frac{5}{16\pi} e^2 Q_0^2 \langle I_i K 20 | I_f K \rangle^2 \quad (3.26)$$

If the 342 keV and 620 keV states in ^{111}Cd are the $\frac{3}{2}^+$ and $\frac{5}{2}^+$ rotational state built on the $\frac{1}{2}^+$ ground state, the ratio of the transition strengths for the transitions to the ground state is given by

$$\frac{B(E2; \frac{5}{2} \rightarrow \frac{1}{2})}{B(E2; \frac{3}{2} \rightarrow \frac{1}{2})} = \frac{\langle \frac{5}{2} \frac{1}{2} 20 | \frac{1}{2} \frac{1}{2} \rangle^2}{\langle \frac{3}{2} \frac{1}{2} 20 | \frac{1}{2} \frac{1}{2} \rangle^2} \quad (3.27)$$

As $\langle \frac{5}{2} \frac{1}{2} 20 | \frac{1}{2} \frac{1}{2} \rangle = \frac{1}{\sqrt{5}}$ and $\langle \frac{3}{2} \frac{1}{2} 20 | \frac{1}{2} \frac{1}{2} \rangle = -\frac{1}{\sqrt{5}}$ the ratio of these transition strengths is

$$\frac{B(E2; \frac{5}{2} \rightarrow \frac{1}{2})}{B(E2; \frac{3}{2} \rightarrow \frac{1}{2})} = 1 \quad (3.28)$$

Thus the $B(E2)$ values in both the weak-coupling model and the particle-rotor model are equal for the $\frac{5}{2}^+ \rightarrow \frac{1}{2}^+$ and $\frac{3}{2}^+ \rightarrow \frac{1}{2}^+$ transitions, i.e. if the states are collective excitations built on the ground state they should have the same transition strengths.

Previous ^{111}Cd and ^{113}Cd results

The nuclei ^{111}Cd and ^{113}Cd are both spin half ground state nuclei attributed to a single odd neutron occupying an $s_{\frac{1}{2}}$ orbit in a spherical shell-model interpretation. They exhibit rather similar nuclear structure. The low lying states of each nucleus are generally identified as single-particle excitations of neutrons to and from single particle orbits of similar energies. In ^{113}Cd a state at 681 keV has been observed and characterised as the odd neutron in the $s_{\frac{1}{2}}$ orbit coupled to the 2_1^+ core excitation in a shell model interpretation [Stu16]. The similar structure of these two nuclei would suggest that a similar state would appear in ^{111}Cd at around the same energy with the same spin. This has been the suggested identification of the purported 754.8 keV $\frac{3}{2}^+$ state in ^{111}Cd . However, in Nuclear Data Sheets two levels have been listed here with energy 752.8 keV and 754.9 keV of spin $\frac{5}{2}^+$ and $\frac{3}{2}^+$, whereas in each of the papers reporting one of these states only one transition is observed [Bla09, Mcd68, Sin85, Koi67]. This suggests a series of errors may have introduced two states into the data sheets while only one level is present in reality.

The g factor is an important tool in determining the structure of the nucleus and has been accurately measured for low lying states in ^{111}Cd . The measured g factors are anomalous, in that the ground state g factor it is approximately half the model value for a spherical nucleus. Previous g -factor results are summarised in table 4.1. The measurement of g factors in higher-excited states gives vital information on how angular momentum is carried in the nucleus. The aim of this work is therefore to measure the g factors for the states corresponding to collective excitations of the core to investigate the nature of these excitations. It has previously been shown that g factors in the odd Cd isotopes are sensitive to the nature of collectivity in the nucleus [Stu16]. In figure 4.1 experimental and theoretical g factors are compared for low-lying states in ^{113}Cd and are shown to disagree with calculations in the particle-vibration model, irrespective of coupling parameter. In contrast, a relatively small quadrupole deformation in a Nilsson-based strong-coupling particle-rotor model brings these values into much better agreement. Similar calculations were performed for analogous states in ^{111}Cd with similar results.

In table 4.2 the expected g factors for an excited $\frac{5}{2}^+$ in ^{111}Cd assuming Schmidt g factors with spin components quenched to 0.7 of the free nucleon value and a core

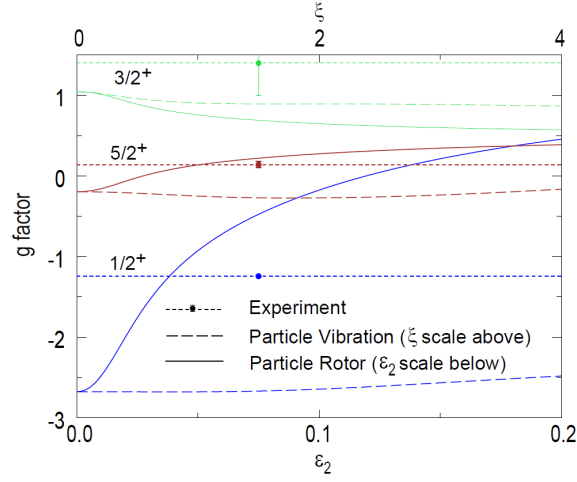


Figure 4.1: Particle-vibrator vs. particle-rotor calculations for ^{113}Cd . g factors are calculated as a function of particle-vibration coupling parameter ξ in the particle vibrator model and as a function of the quadrupole deformation ϵ_2 in the particle rotor model. Experimental values are plotted with dotted lines and points to indicate measurement errors. Figure taken from Ref. [Stu16].

component of $\frac{Z}{A}$. The calculated values may be compared to experimental values to identify the configuration of the nucleus.

Measurements of $B(E2)$ values as displayed in table 4.3 clearly show collectivity in the 342 keV, 620 keV, and 752.8 keV state, with the 245 keV state exhibiting single particle structure, as noted in section 3.3.

Applying the results of section 3.7, the 342 keV state and the 620 keV state have $B(E2) \downarrow$ values of $B(E2; \frac{3}{2} \rightarrow \frac{1}{2}) = 15.4(8)$ and $B(E2; \frac{5}{2} \rightarrow \frac{1}{2}) = 14.0(11)$, respectively. As their ratio is consistent with unity these results are consistent with these states being either the two couplings of the ground state to the core vibrational phonon, or members of the rotational band built on the ground state.

Table 4.1: Previous experimental g factors with identification in a particle-vibration model.

Excitation energy (keV)	I^π	Configuration identification	g factor
0	$\frac{1}{2}^+$	$s_{\frac{1}{2}} \otimes 0^+$	-1.1898 ^a
245.2	$\frac{5}{2}^+$	$d_{\frac{5}{2}} \otimes 0^+$	-0.306(1) ^a
342.1	$\frac{3}{2}^+$	$d_{\frac{3}{2}} \otimes 0^+$	0.6(4) ^b
620.2	$\frac{5}{2}^+$	$s_{\frac{1}{2}} \otimes 2^+$	0.21(4) ^b

^a Data from Nuclear Data Sheets, Ref. [Bla09].

^b Data from Ref. [Stu16].

Table 4.2: Simple Landé addition calculations for $\frac{5}{2}^+$ states assuming quenching of the odd particle to 0.7 of the free value and core g -factor $\frac{Z}{A}$

Coupled states	Quenched single particle g factor	Expected g factor
$d_{\frac{5}{2}} \otimes 0^+$	-0.536	-0.536
$s_{\frac{1}{2}} \otimes 2^+$	-2.678	-0.190
$d_{\frac{5}{2}} \otimes 2^+$	-0.536	-0.204
$d_{\frac{3}{2}} \otimes 2^+$	0.536	0.471
$g_{\frac{7}{2}} \otimes 2^+$	0.298	0.290

Table 4.3: Experimental $B(E2)$ values for low-lying states in ^{111}Cd .

Transition energy (keV)	Spin	$B(E2)\downarrow$ (W.u.)
245.2	$\frac{5}{2}^+$	0.29(2) ^a
342.1	$\frac{3}{2}^+$	15.4(8) ^a
620.2	$\frac{5}{2}^+$	14.0(11) ^a
752.8	$\frac{5}{2}^+$	4.4(8) ^b

^a Data from Ref. [Sin85]

^b Data from Ref. [Mcd68]

Thin-foil IMPAC technique

5.1 The Transient Magnetic Field

In order to investigate the magnetic properties of the nucleus a strong magnetic field is required. Typical nuclear states have lifetimes (τ) of a few picoseconds. It is therefore difficult to create a large enough static field in the lab to cause a measurable precession angle, $\Delta\theta = \omega_L\tau$,

$$\omega_L = -gB\frac{\mu_N}{\hbar} \quad (5.1)$$

where B is the magnetic field at the nucleus and μ_N is the nuclear magneton. However, ions moving through a polarized ferromagnetic material experience a strong *transient magnetic field* of the order of several thousand Tesla. As the ion moves rapidly through the medium it experiences an effective field in the direction of the polarization of the ferromagnetic medium with a magnitude of a few kT, and that behaves like an external field. As the ion moves through the medium it captures electrons into its s orbits. As the electrons around the nucleus are polarized in the medium generally electrons of that spin are captured into these states. The reduced numbers of electrons of opposite polarization tend to extend the lifetimes of these states. Strong fields are introduced by the overlap in the wavefunctions of the $s_{\frac{1}{2}}$ orbits and the nucleus, the so called Fermi contact field.

Much work has been done to characterise the magnetic field empirically as an analytical prediction is difficult. In this work a parametrization of the transient magnetic field determined by detailed studies on Pd ions was used [Stu98]. This has been shown to be accurate for heavy ions implanted into iron hosts as were used in this experiment [Cha11].

$$B_{TF} = aZ^{p_Z}\left(\frac{v}{v_0}\right)^{p_V} \quad (5.2)$$

where p_Z and p_V are parameters specific to the ion and host, a is the host-dependent scale parameter, v is the velocity of the ion, and $v_0 = \frac{c}{137}$ is the Bohr velocity. The parameters are generally of the order $p_Z \approx 1$ and $p_V \approx 0.45$. In this region a faster velocity is preferable to create a larger magnetic field.

5.2 The Ion Implantation Perturbed Angular Correlation (IMPAC) technique

In IMPAC experiments an excited nucleus is implanted into a polarized ferromagnetic material in which it slows, experiencing a strong transient magnetic field. As it slows the distribution precesses about the magnetic field by an angle $\Delta\theta$. When the nucleus stops in the ferromagnetic material it continues to precess due to the weaker field used to polarize the electrons and a field due to the host on the nucleus. In order to account for the decay of the nucleus exponential decay terms are added and the angular change becomes

$$\Delta\theta = -g\frac{\mu_N}{\hbar}\left(\int_0^{T_{stop}} B_{tr}(t)e^{-t/\tau}dt + B_{st}\tau e^{-T_{stop}/\tau}\right) \quad (5.3)$$

where B_{tr} is the transient magnetic field, B_{st} is the static magnetic field, and T_{stop} is the time taken for the excited nucleus to stop in the host. It is important to note that the static field may add or cancel the transient-field component. These effects are often not well characterised and so it may not be possible to determine the g factor from $\Delta\theta$. In order to avoid ambiguities from the static interaction, which can cancel out the transient-field effect, the thin-foil IMPAC technique was developed.

5.3 Thin-foil IMPAC experiments

In thin foil experiments three-layered targets are used. In the present work the thin first layer was the isotope of interest ^{111}Cd . The target nucleus is Coulomb excited and recoils through the second ferromagnetic layer to stop in the non-magnetic third. The second layer is a thin layer of ferromagnetic material polarized by an external magnetic field, in this case iron. The third layer is a thick non-magnetic backing in which the recoiling nucleus stops and does not precess; here we have used copper.

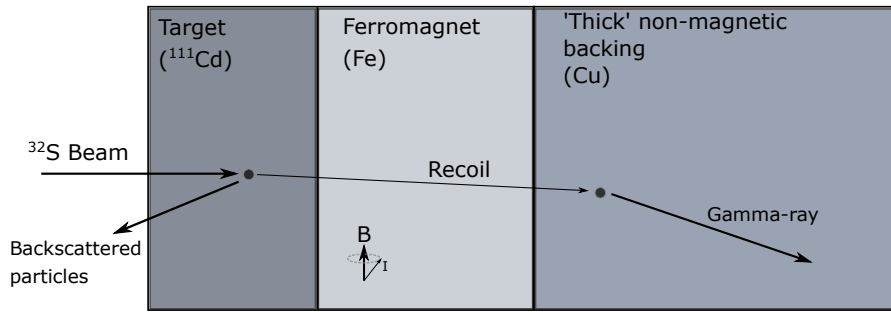


Figure 5.1: Three-layered target diagram showing the target layer, the ferromagnetic layer, and the non-magnetic backing.

This arrangement solves two problems, firstly, the lifetime for the state need not be

known precisely provided that it is significantly longer the time taken to pass through the ferromagnetic layer. The time taken to cross this section is of the order of hundreds of femtoseconds ($\lesssim 1$ ps). In this case of $\tau \gg T$, the formula for the total precession simplifies significantly.

$$\Delta\theta = -g \frac{\mu_N}{\hbar} \int_0^T B_{tr}(t) dt \quad (5.4)$$

The time taken for the nucleus to stop has been replaced with the transit time through the ferromagnetic layer (T). In order to determine $\Delta\theta$ experimentally the difference in counts in two detectors at equivalent angles $\pm\theta_\gamma$ is measured for fields in the ‘up’ and ‘down’ directions. We define the number of counts in a gamma ray detector for a field direction in terms of the angular distribution $W(\theta)$ and the total number of gamma decays in coincidence with detected particles, and use the symmetry of the angular distribution around 0° to write

$$N_{1\uparrow} = N_{1\uparrow}^0 W(\theta_\gamma - \Delta\theta) \quad (5.5a)$$

$$N_{2\uparrow} = N_{2\uparrow}^0 W(\theta_\gamma + \Delta\theta) \quad (5.5b)$$

$$N_{1\downarrow} = N_{1\downarrow}^0 W(\theta_\gamma + \Delta\theta) \quad (5.5c)$$

$$N_{2\downarrow} = N_{2\downarrow}^0 W(\theta_\gamma - \Delta\theta) \quad (5.5d)$$

The numbers 1, 2 indicate which gamma ray detector, N_1 is at $+\theta_\gamma$, N_2 is at $-\theta_\gamma$; the arrows indicate field direction and $N_{i\uparrow}^0$ is the total number of gamma decays in the transition for that field direction with particle detections and accounting for detector efficiency. We now define the double ratio ρ .

$$\rho = \sqrt{\frac{N_{1\uparrow}}{N_{1\downarrow}} \cdot \frac{N_{2\downarrow}}{N_{2\uparrow}}} = \frac{W(\theta_\gamma - \Delta\theta)}{W(\theta_\gamma + \Delta\theta)} \quad (5.6)$$

The $N_{i\uparrow}^0$ factors cancel as the dependence on field direction is through integrated beam current, which is the same for each detector. Likewise differences in detection efficiency cancel due to the ratios of \uparrow / \downarrow . As $\Delta\theta$ is small it is possible to Taylor expand this to first order with great accuracy.

$$\rho = \frac{W(\theta_\gamma) - \Delta\theta \left. \frac{dW}{d\theta} \right|_{\theta_\gamma}}{W(\theta_\gamma) + \Delta\theta \left. \frac{dW}{d\theta} \right|_{\theta_\gamma}} \quad (5.7)$$

In order to simplify notation the ‘slope’ is defined as

$$S = \frac{1}{W(\theta_\gamma)} \left. \frac{dW}{d\theta} \right|_{\theta_\gamma}. \quad (5.8)$$

Thus

$$\rho = \frac{1 - S\Delta\theta}{1 + S\Delta\theta}. \quad (5.9)$$

Defining the ‘effect’

$$\epsilon = \frac{1 - \rho}{1 + \rho} \quad (5.10)$$

gives

$$\Delta\theta = \frac{\epsilon}{S}. \quad (5.11)$$

Using this formula along with equation 5.4 provides the expression

$$g = \frac{\epsilon}{S\phi}, \quad (5.12)$$

where

$$\phi = -\frac{\mu_N}{\hbar} \int_0^T B_{tr}(t) dt = \frac{\Delta\theta}{g} \quad (5.13)$$

To sum up, formulating the analysis in terms of a double ratio is useful in ensuring that the results of the experiment are not affected by several sources of systematic error. Changes in beam current over time and differing times with the field ‘up’ and ‘down’ are accounted for by the ratio. It has also been shown that the double ratio is insensitive to slight misalignment between angles for gamma-ray detector pairs [Stu82].

Experimental method

6.1 Target preparation

The targets for thin-foil IMPAC experiments are three layered targets as previously described. The first layer of the target in this work was 95% enriched ^{111}Cd , 0.36 mg/cm^2 thick; the second layer was 2.469 mg/cm^2 ^{Nat}Fe , and the third layer is a “thick” natural copper backing, $12 \mu\text{m}$ thick. Isotopic fractions in the separated isotope Cd are given in table 6.1. Cadmium has a low melting point at 321°C so in order to ensure that this remained on the target care was taken in ensuring the target was not heated excessively both during target preparation and during the experiment.

Table 6.1: Isotopic fractions of the ^{111}Cd separated isotope.

Isotope	Atomic percent	Precision	2^+ Excitation energy (keV)
^{106}Cd	0.02	0.02	632.6
^{108}Cd	0.03	0.02	633
^{110}Cd	0.63	0.02	658
^{111}Cd	95.29	0.10	-
^{112}Cd	2.61	0.05	617.5
^{113}Cd	0.49	0.02	-
^{114}Cd	0.71	0.02	558.5
^{116}Cd	0.22	0.02	513

Target preparation took place in several stages. The first involved cleaning and annealing the Fe foil, the second was electroplating of the separated isotope of ^{111}Cd onto the Fe foil. Finally, the Cu backing was attached by evaporating a layer of indium onto both the back of the iron foil and the ‘front’ of the Cu foil. These were then pressed together ($\lesssim 2$ Tonne pressure) such that the indium served as an adhesive between the iron and copper layers. During the evaporation process the iron with the plated ^{111}Cd was kept at a greater distance from the heated indium in order to maintain the bond between the ^{111}Cd and the ^{Nat}Fe .

An iron foil of the correct thickness was obtained from Goodfellow metals. To anneal it, it was placed in a tantalum holder in the vacuum chamber of an evaporator as in figure 6.1b. This chamber was evacuated and the foil was heated to 850°C for 20 minutes. This annealed the iron layer for the target, creating a uniform lattice, enlarging magnetic domains and cleaning the surfaces.

The available ^{111}Cd was in oxide form. In order to make a pure ^{111}Cd target this CdO was dissolved into a 5% solution of acetic acid. In industrial electroplating of Cd, CdO is dissolved in alkaline cyanide solutions. In this work it was shown that Cd readily dissolves in a non-toxic acetic acid solution. This process is suitable for small-scale electroplating for the creation of nuclear targets. The ^{111}Cd in the acetic acid solution was then electroplated onto the annealed iron using the plating cell illustrated in figure 6.1a. Initially, difficulties arose as the bonding of the ^{111}Cd to the iron was insufficient while significant dendritic reduction of the Cd occurred, however lowering current significantly ameliorated these issues and a uniform ^{111}Cd target was created, after some trial and error with natural CdO material. It must be noted that although Cd has a low melting point, and would seem to be ideal for target preparation by evaporation, as it evaporates readily, it does not adhere well to backing media, thus making the method unsuitable for expensive separated isotope.

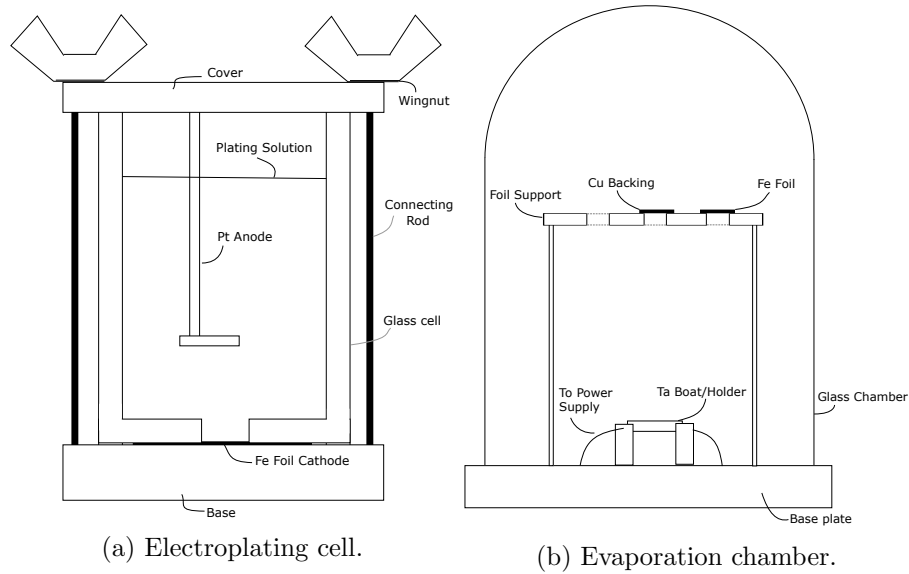


Figure 6.1: Diagrams of equipment used in target preparation. The tantalum boat was replaced with a rectangular tantalum holder for the annealing process.

6.2 The ANU hyperfine spectrometer

The study of the magnetic properties of ^{111}Cd was performed using the ANU hyperfine spectrometer shown in figure 6.2. A small electromagnet was used to polarize the Fe in

the target. The target was placed on the target mount connected to a cold finger. The cold finger acts to keep the target at a temperature of 6 K utilizing a cryocooler while the beam is on the target. This helps to completely polarize the ferromagnetic material and keeps the cadmium from evaporating from the target even with intense beams.

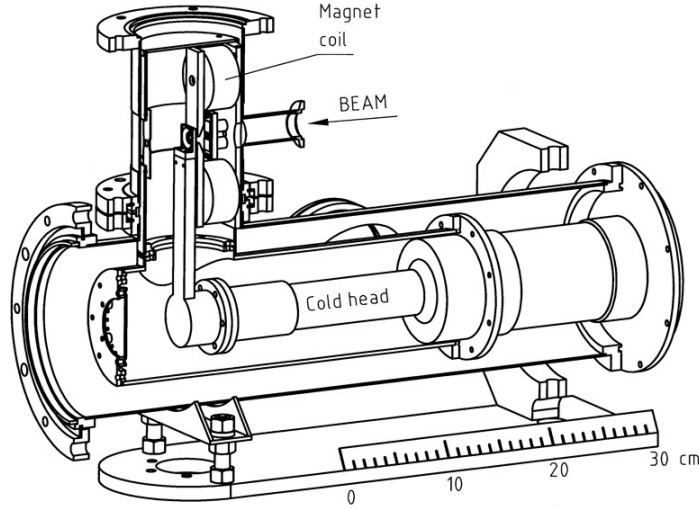


Figure 6.2: Diagram of hyperfine spectrometer target chamber. Figure drawn by Allan Harding (ANU).

6.3 Beam properties

In choosing the beam properties several factors must be taken into account. The first thing to note is that the faster the target ion recoils, the larger the transient magnetic field that is experienced, and the thicker the ferromagnetic layer may be. Both cause larger precessions of the angular correlations, thus improving the fractional error for given statistics. Increasing the energy of the beam will cause faster recoils, however, as the energy of the beam approaches the Coulomb barrier energy, fusion begins to occur. This increases the background and the gamma detection rate of unwanted radiation. Raising the gamma detection rate causes pile-up effects and can overload the data acquisition system so the energy must remain below barrier energies on Cd, Fe, and Cu. The two considered beam species were ^{32}S and ^{58}Ni . The higher Z value of the nickel raises the barrier energy and so a higher beam energy can be employed, however its higher mass reduces its backscatter energy. The backscatter energy is important as this nucleus must be registered by the particle detector. Ensuring that the backscattered particles were detected was determined more important, and so ^{32}S was chosen at a beam energy of 90 MeV. Experience gained in Ref. [Stu81] was considered in making this decision.

6.4 Detector setup

The setup included four High Purity Germanium (HPGe) gamma ray detectors and two rectangular silicon photodiode particle detectors. The silicon detectors were placed at back angles near 150° with respect to the beam axis above and below the beam axis. The positioning of the detectors is shown in figure 6.3.

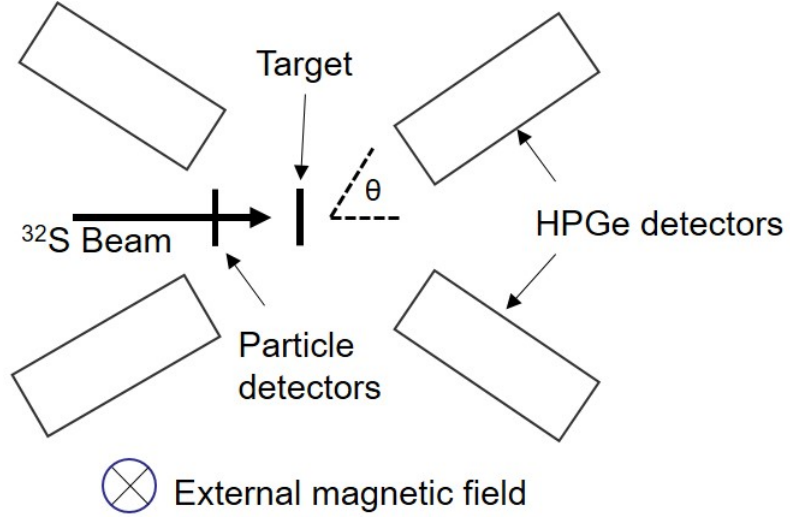


Figure 6.3: Diagram of the angular correlation station. All angles stated in this thesis are defined as in this diagram. The beam is along 0°

The beam current on target could not be directly measured as the target is mounted on the cryocooler and is thick so that the accelerated beam is stopped in the Cu layer, so, to maximise the flux on the target, and the rate of data collection, the rate of backscattered particle detections was maximised.

The advantage of HPGe detectors over scintillators is their superior energy resolution, which allowed the individual identification of transitions close in energy. This was important to distinguish whether a single peak or two peaks were present at 752.8 keV and 754.9 keV. The resolution of the detectors in this region was ~ 2 keV FWHM, therefore the two peaks should clearly be seen if present.

6.4.1 Angular correlation gamma-ray detector setup

In the angular-correlation measurements one backward gamma ray detector was kept at a constant position so that the number of counts in each peak can be normalised for the amount of time the detectors spent at each position. The other detectors were moved to several angles to measure the relative number of decays as a function of angle.

6.4.2 g -factor measurement gamma detector setup

The placement of the gamma-ray detectors in the g factor measurements must be considered to minimise the uncertainty in $\Delta\theta$. Assuming an approximately equal number of gamma detections in each detector for each field direction, N , we arrive at an estimate of the uncertainty in $\Delta\theta$, $\sigma_{\Delta\theta}$:

$$\sigma_{\Delta\theta}^2 \approx \frac{1}{4S^2N}. \quad (6.1)$$

In order to minimise this quantity we this want to maximise the sensitivity S^2N , or equivalently S^2W , where S is the slope as defined in Section 5.3 and W the angular correlation. The sensitivity for the 752.8 keV transition is displayed in figure 6.4 assuming a pure E2 transition. Clearly the optimum detector placement occurs around $\theta_\gamma = 65^\circ$.

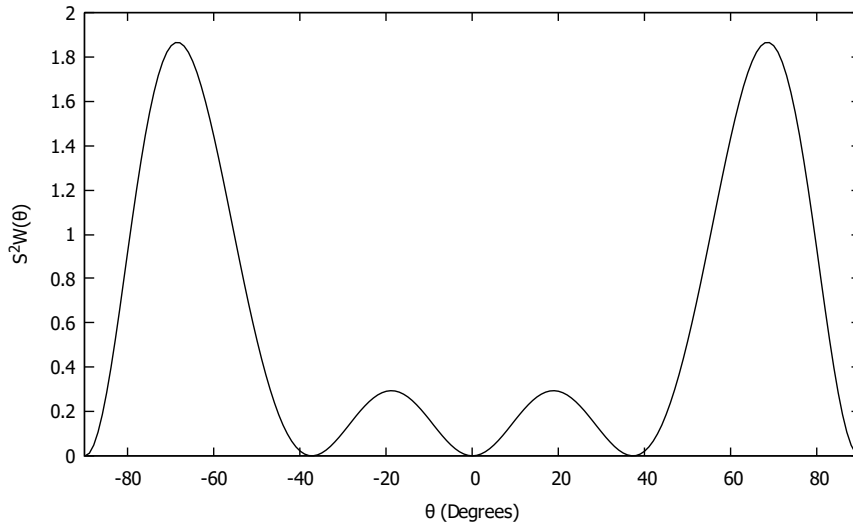


Figure 6.4: Sensitivity of g -factor measurement $S^2W(\theta)$ assuming a pure E2 transition. The optimum detector placement occurs at the maxima, in this case at $\theta_\gamma = 65^\circ$.

Upon observing an $E2$ shape in preliminary analysis of the 752.8 keV transition, the g -factor measurements were performed with the four gamma ray detectors at 65° , 115° , 245° , and 295° , due to the symmetries of the angular distribution across 0° and 90° , these are each effectively at $\theta_\gamma = 65^\circ$. The detectors used for the front pair, and the back pair are very similar in crystal size and performance, these create well-matched pairs for the analysis process described to determine the g factor.

6.5 Analysis electronics

Data for gamma spectroscopy experiments are taken as coincidence events triggered by a master gate. Events are defined when either of the particle detectors registers a particle and one of the gamma-ray detectors also registers a gamma ray within ~ 800 ns. An overlap in logic signals from any particle with any gamma forms the master gate. Each

event is written with a gamma ray energy for each detector, a particle energy for each detector, a time difference between any particle detection and each gamma detection or particle detection, and the field direction for that event.

A diagram showing detection electronics is displayed in figure 6.5. The fast pulse timing signal from the detector is shaped with a timing filter amplifier (TFA) before passing through a constant fraction discriminator (CFD) which creates an inverted copy of the signal, delays it by a fraction of the rise time, and adds it to the original signal. This is done so that the zero crossing is at the same point in each pulse regardless of the original pulse height. This new pulse is then sent to a time-to-digital converter (TDC). In the case of particles this effectively acts to label the particle detector that is associated with the event, this is then used to avoid events from simultaneous particle detections. The timing from the HPGe detectors is used to create a time difference between the particle detection and gamma detection, which can be used to determine which events correspond to real Coulomb excitation reactions and which are in random coincidence.

The energy signal from the detectors is sent through an amplifier in which it is shaped into a gaussian. This shaped signal is sent to an analog-to-digital converter (ADC) which converts the pulse height into a digital signal to be registered by the data acquisition system.

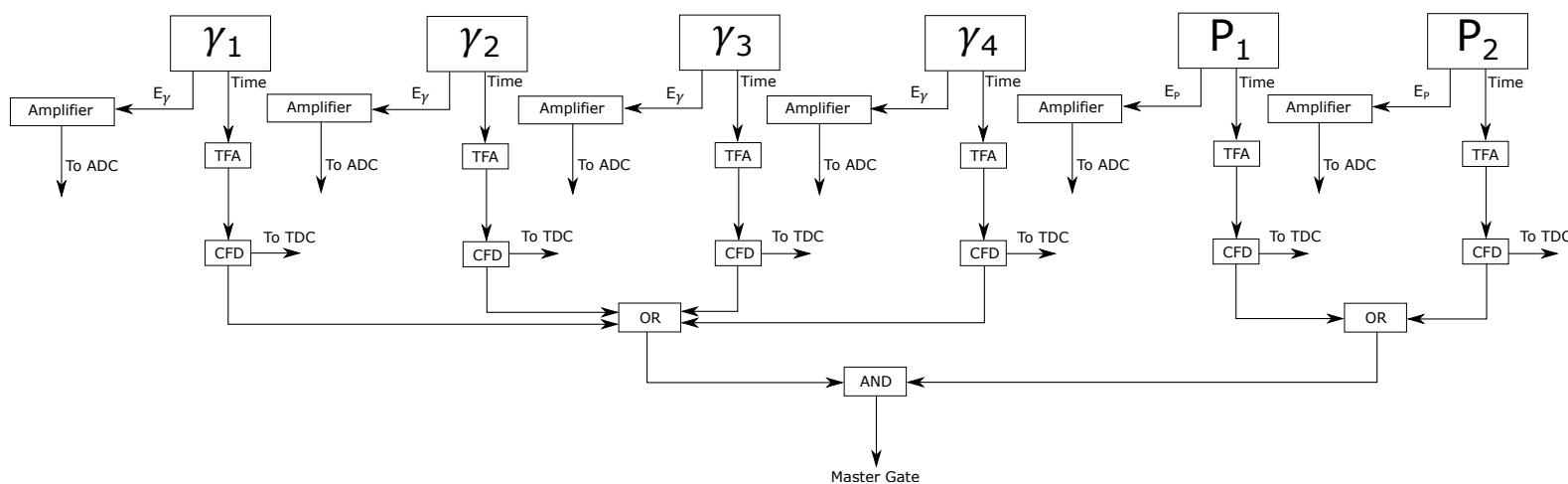


Figure 6.5: Diagram of pulse processing electronics. Events are only recorded when the coincidence requirement of any particle and any gamma within 800 ns is met.

6.6 Sorting, gating, and subtractions

During the experiment, data is collected event-by-event in so called list mode. Continuing to analyse data on an event-by-event basis after the experiment, however, is computer intensive and unnecessary. Instead sorts are performed in order to bin the data of interest into a few relevant histograms (usually spectra of counts versus energy). The event data was therefore sorted into spectra showing the particle-gamma time difference for each detector, the number of particles of each energy, and the particle detection time. The event data for the gamma energy spectrum could then be sorted only allowing relevant information by gating on the regions of interest.

The ^{111}Cd was thin enough that the energy distribution from these scattering events form a well defined peak separated from the other particle energies and noise. As the ^{111}Cd is higher mass than the iron and copper, the energy of the backscattered particles is higher from the ^{111}Cd than for the other nuclei. As such there is very little background in this spectrum and counts from the other scattering events can be ignored by gating on particle energy in the sorting process. Similarly, the time difference between particle detection and gamma detection changes very little between non-isomeric states and so a clear peak is seen in the time difference spectrum, figure 6.7. These times can be gated on to select true coincidences, in addition, the constant background here also allows an estimate of, and correction for, random coincidences within the ‘true’ gate region as seen in figure 6.7.

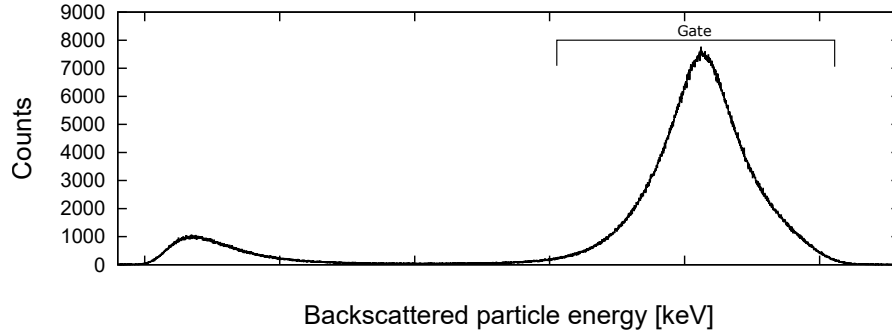


Figure 6.6: Experimental particle energy spectrum. The peak shown is for backscattered particles from the ^{111}Cd and the example gate covers the range of interest.

The combination of the coincidence requirement with particles of the correct energy and the clean time difference peak for background subtraction allowed the production of clean gamma-ray energy spectra.

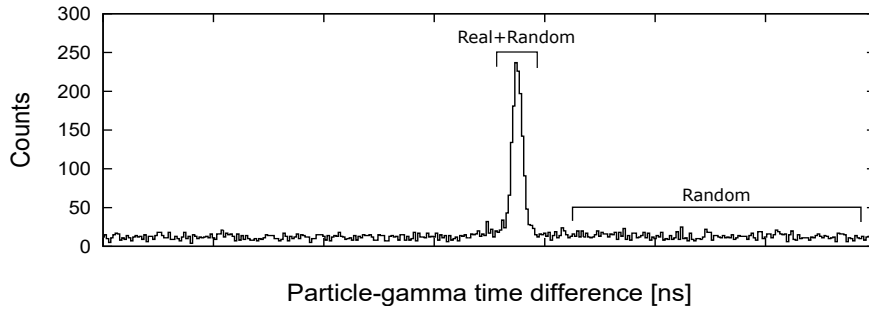


Figure 6.7: Experimental particle-gamma time difference spectrum. The “real” region contains gamma-rays from true Coulomb excitation events. The “random” region was used to estimate the background under the peak.

6.7 Energy calibration and angular efficiency calibration

Immediately after the conclusion of the g -factor measurements a ^{152}Eu source was placed in the target position. Events were then recorded as singles events (no longer in coincidence with particle detection). The HPGe detectors were then placed in the same positions as in the angular correlation experiments allowing the relative efficiency of the detector to be determined at each of these positions. Accounting for the angular efficiency was important in this experiment as at zero degrees the gamma decays were passing through a beam stop which stops any beam which passes through the target, and consists of a lead foil. Absorption of gamma rays in the Pb stop lowers the detector efficiency at this angle.

Observed spectra and angular correlations

7.1 Transitions and level structure

7.1.1 Observed transitions

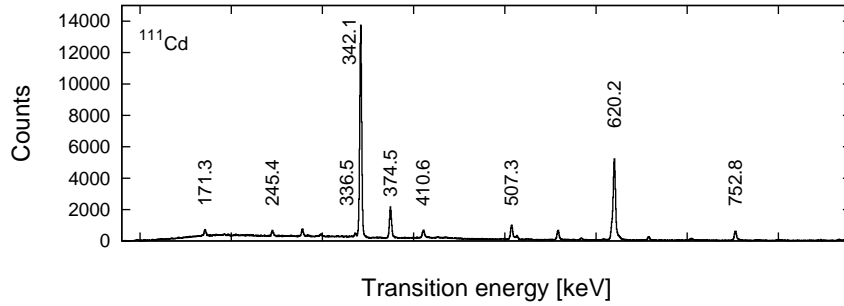


Figure 7.1: Experimental gamma-ray spectrum with strong peaks from collective states clearly visible on a linear scale.

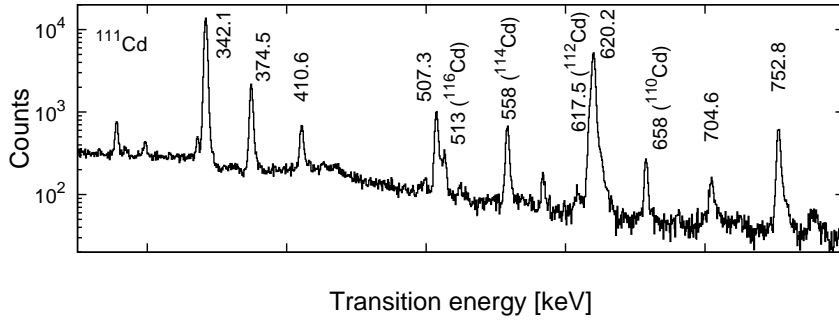


Figure 7.2: Experimental gamma ray spectrum on log scale.

A full list of observed transitions from ^{111}Cd is displayed in table 7.1. The strongly excited states were found to be 342 keV, 620 keV and 752.8 keV with the largest intensity observed for the 342 keV decay. The strong excitation of these levels in Coulomb excitation is indicative that the states are collective in nature. The strong excitation of

each of these levels has long been known however the strong excitation of the 342 keV level does not fit with a single particle excitation to the $d_{3/2}$ orbit. A comparison between the observed level scheme in the present work and in Nuclear Data Sheets is displayed in figure 7.3.

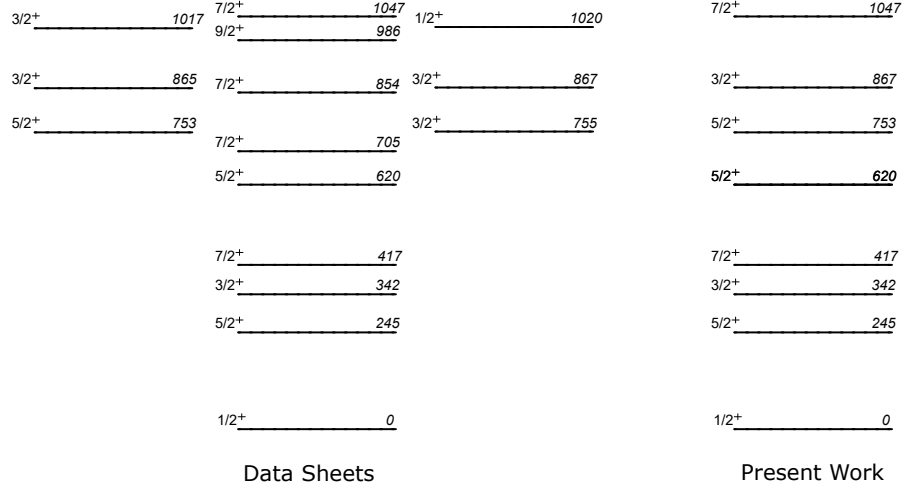


Figure 7.3: Observed level scheme comparison with Nuclear Data Sheets, Ref. [Bla09].

7.1.2 Doppler broadening

States with shorter lifetimes may decay in flight, Doppler shifting the emitted gamma rays. Doppler shifts are governed by the equation

$$E_\gamma = E_{\gamma 0} \left(1 + \frac{v}{c} \cos \theta \right) \quad (7.1)$$

where $E_{\gamma 0}$ is the energy of the transition, E_γ is the detected energy, v is the velocity of the decaying nucleus, and θ is the angle between the direction of motion of the nucleus and the gamma-ray emission. Doppler broadened lineshapes were observed for several transitions including the gamma rays from each of the decays out of the 752.8 keV state and the decays out of the 620 keV state. The presence of these Doppler-shifts indicates that the nucleus is in motion during some gamma-ray decays, and hence that the lifetime is of the order of the stopping time which is ~ 1 ps. Doppler broadened lineshapes may be fit for a known velocity to find the average time for a given decay. The similar lineshapes for the transitions to the ground state from each of these states suggests a similar lifetime for each of these states, however the method is complex to do properly and such an analysis is beyond the scope of this present project.

Table 7.1: Observed transitions, level energies and spins taken from Nuclear Data Sheets [Bla09].

E_i (keV)	I_i	E_γ (keV)	E_f (keV)	I_f	Multipolarity	Relative intensity (65°)
0	$\frac{1}{2}^+$		0			
245.4	$\frac{5}{2}^+$	245.4	0	$\frac{1}{2}^+$		
342.1	$\frac{3}{2}^+$	342.1	0	$\frac{1}{2}^+$	M1+E2	1000(4)
		96.75	245.4	$\frac{5}{2}^+$		
416.7	$\frac{7}{2}^+$	171.3	254.4	$\frac{5}{2}^+$		
620.18	$\frac{5}{2}^+$	620.2	0	$\frac{1}{2}^+$	E2	660(5)
		374.5	245.4	$\frac{5}{2}^+$		163(2)
		277.9	342.1	$\frac{3}{2}^+$		27(1)
		203.2	416.7	$\frac{7}{2}^+$		
752.8	$\frac{5}{2}^+$	752.8	0	$\frac{1}{2}^+$	E2	105(2)
		507.3	245.4	$\frac{5}{2}^+$	M1+E2	113(2)
		410.6	342.1	$\frac{3}{2}^+$	M1+E2	47(2)
		336.5	416.7	$\frac{7}{2}^+$	M1+E2	16(2)
866.6	$\frac{3}{2}^+$	866.1	0	$\frac{1}{2}^+$		18(1)
		524.2	342.1	$\frac{3}{2}^+$		
1046.8	$(\frac{7}{2}^+)$	801	245.4	$\frac{5}{2}^+$		15(1)
		704.9	342.1	$\frac{3}{2}^+$		22(1)

7.1.3 Angular correlations

Angular correlation were measured for several transitions and results are shown in figure 7.4. Spin assignments for the 620 keV and the 342 keV state can be confirmed, with an $E2$ transition for the 620 keV transition and an $E2/M1$ correlation for the 342 keV transition. The literature mixing ratio for the 342 keV of 0.36 has been used in the fit for the angular correlation shown in the figure and has been confirmed. As shown in table 6.1, the largest contaminant in the ^{111}Cd sample is ^{112}Cd with a 2^+ excitation energy of 617.5 keV. To measure the angular correlation of the 620 keV transition from ^{111}Cd it was therefore necessary to also fit the 617.5 keV transition from ^{112}Cd .

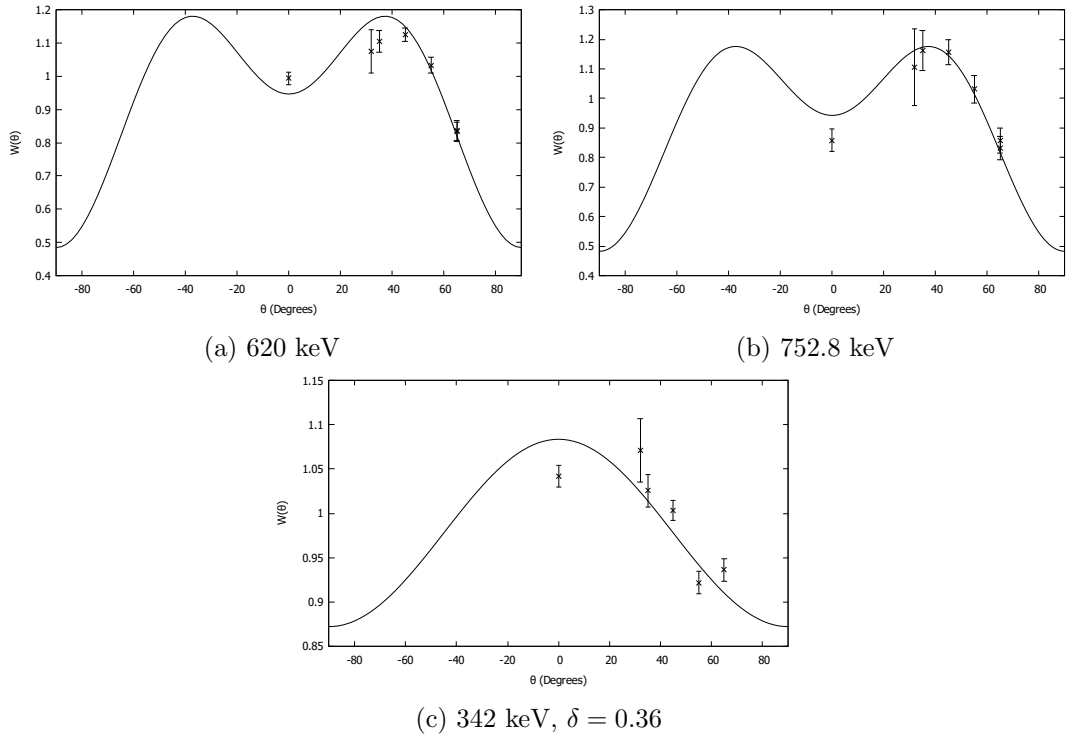


Figure 7.4: Angular correlations for the 342 transition transition, the 620 keV transition, and the 752.8 keV transition, the 620 keV and 752.8 keV transition have clear $E2$ correlations while a good fit is obtained for the 342 keV transition with the literature mixing ratio of 0.36 [Bla09]

The 0° points of these angular correlations are consistently low, however this point is high for the 620 keV peak suggesting that the number of counts in this peak was anomalously high in the runs with the detector at 0° , thus lowering other points in the normalisation process.

The angular correlation for the 752.8 keV transition has a clear $E2$ shape with a non-zero A_4 coefficient. This indicates that the spin is $\frac{5}{2}^+$ as the states differ by two units of angular momentum. A transition from a $\frac{3}{2}^+$ state would be a mixed transition

and have $A_4 = 0$. The result here challenges the particle-vibration model as no state corresponding to the 2^+ coupling with the ground state to $\frac{3}{2}^+$ was strongly Coulomb excited.

7.2 Lifetime curve

The lifetime curve measured for the 245 keV transition is displayed below. The half-life for this state is measured to be 83(10) ns in good agreement with the literature value of 84.5(4) ns. The line indicates the 84.5(4) ns literature value for the half-life. The error in this value is quite large due to a lack of counts. Coulomb excitation was not ideal for this measurement as the low $B(E2)$ value from the single particle limits the population of, and hence decays from this state.

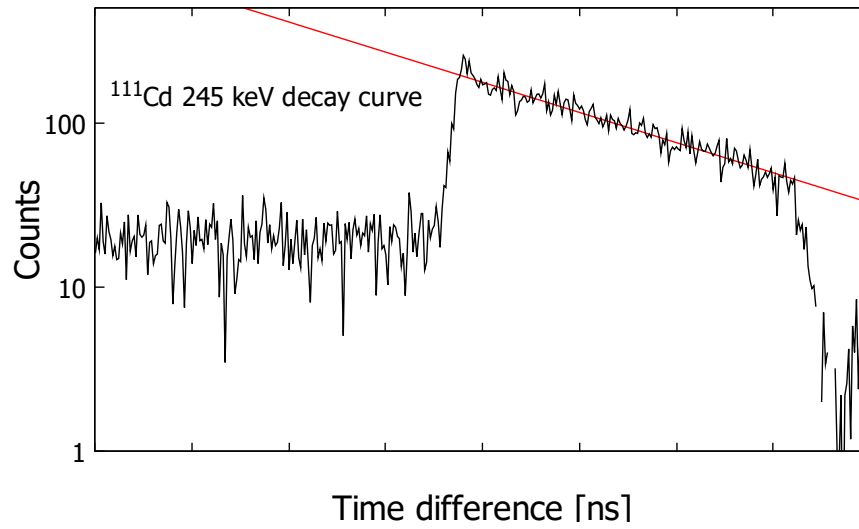


Figure 7.5: Decay curve for the 245 keV transition. The line plots the expected decay with $T_{\frac{1}{2}} = 84.5$ ns.

The result is shown here as a confirmation of the measurement and analysis procedures employed.

g factor results

Measurements were made of the g factors of the 342 keV, 620 keV, and 752.8 keV states. The measurements for the 342 keV state has improved precision over previous measurements, while the g factor for the 752.8 keV state had not previously been measured. Values obtained in this experiment are presented in table 8.1.

Table 8.1: Experimental g factors in ^{111}Cd .

E (keV)	I_i^π	$\epsilon \times 10^3$	S (rad $^{-1}$)	$\Delta\theta$ (mrad)	g^a	g^b	g^c
342.1	$\frac{3}{2}^+$	+8(2)	-0.18(4)	-45(13)	+0.9(3)	+0.6(4)	+0.03(110)
620.2	$\frac{5}{2}^+$	+14(5)	-1.43(7)	-10(4)	+0.21(8)	+0.25(7)	+0.15(6)
752.8	$\frac{5}{2}^+$	+31(11)	-1.43(10)	-22(8)	+0.46(16)		

^a Present values

^b Ref. [Stu16]

^c Ref. [BK89]

A reduced error in the g -factor measurement for the 620 keV state may be possible with a more sophisticated subtraction method for removing the 617.5 keV state. The strong Doppler broadening observed for this state significantly hindered accurate fitting of peak components. Nevertheless, each g -factor measurement in the present work agrees with previous measurements within uncertainties, thus confirming that the employed procedures are sound. The value for the previously unmeasured 752.8 keV state clearly indicates a positive g factor. As will be evident in the following discussion, the signs of the g factors are crucial in distinguishing particle-vibration versus particle-rotor behaviour.

Discussion and interpretation

9.1 Particle-vibration calculations and interpretation

9.1.1 Predictions of energy levels

As described in Section 2.3.4, calculations were performed for ^{111}Cd assuming a harmonic vibrator core coupled to the unpaired neutron. The initial calculation was performed with the vibrational phonon energy set to the excitation energy of the first 2^+ state of the neighbouring ^{112}Cd nucleus, $\hbar\omega = 618$ keV. The parameters were then allowed to vary to find the best fit to the experimental energy spectrum. A good fit was found with a particle coupling parameter of 0.56 and a phonon energy of $\hbar\omega = 550$ keV. Similar parameters were found in previous work [Stu16]. The results of this fit are exhibited in figure 9.1.

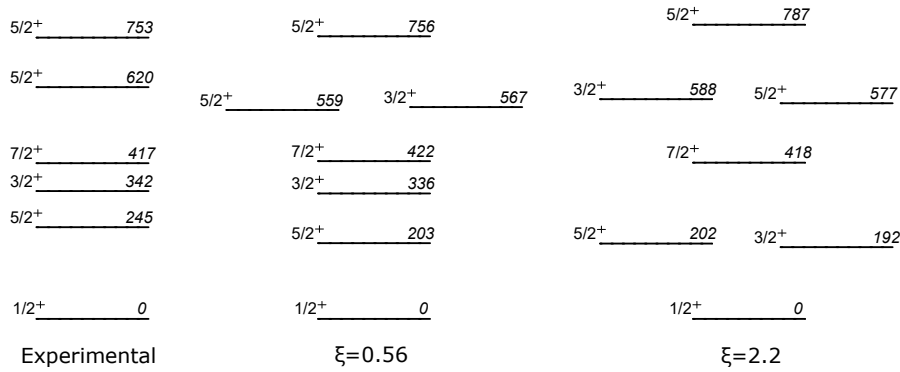


Figure 9.1: A comparison between the levels observed in this experiment and calculated particle-vibration level schemes for parameters $\xi = 0.56$, $\hbar\omega = 550$ keV and, $\xi = 2.2$, $\hbar\omega = 440$ keV.

In the particle-vibration model we expect to see low lying $d_{3/2}$ and collective $\frac{3}{2}^+$ ($s_{1/2} \otimes 2^+$) states. The predicted energy for the $\frac{3}{2}^+$ state corresponding to the 2_1^+ core excitation is calculated to be of a similar energy to the observed 620 keV level. If a collective state existed at this energy it would be strongly Coulomb excited. The

possibility that this state was excited and the decay was hidden within the broadened 620 keV peak was considered, however, the accurate fit of the angular correlation to an $E2$ shape suggests that no $M1/E2$ transition from a $\frac{3}{2}^+$ state (with no A_4 term) is under the 620 keV transition. It was therefore concluded that the collective $\frac{3}{2}^+$ state predicted by the particle-vibration model was not present.

9.1.2 g factor comparison

As discussed in section 3.3 the lowest excited state in ^{111}Cd is an isomeric $\frac{5}{2}^+$ state. The g factor is consistent with a state of predominantly $d_{5/2}$ parentage, however in shell model calculations the lowest single-particle excitation should be to the $d_{3/2}$ orbit. In order to model the observed level structure the energy of the $d_{5/2}$ orbit was lowered to ~ 200 keV. While this allows the energies in the level structure to be accurately fitted there is little theoretical backing to support setting the orbital energy to this value.

A further problem with the particle-vibration model concerns the sign of the g factors for the $\frac{5}{2}^+$ and $\frac{5}{2}^+$ states. The predicted g factors, using the parameters stated above, are negative for the 620 keV and 752.8 keV states, while the experimental g factors are positive by over two standard deviations. Parameter combinations were further investigated and it was found that increasing the coupling parameter ξ can cause the g factor for the $\frac{5}{2}^+$ state at 752.8 keV to become positive, although as previously reported, the g factor of the $\frac{5}{2}^+$ never becomes positive. Further, the predicted g factor for the ground state is twice the experimental value. The relationship between the coupling parameter and the g factors for the ground state and excited $\frac{5}{2}^+$ states are displayed in figure 9.2.

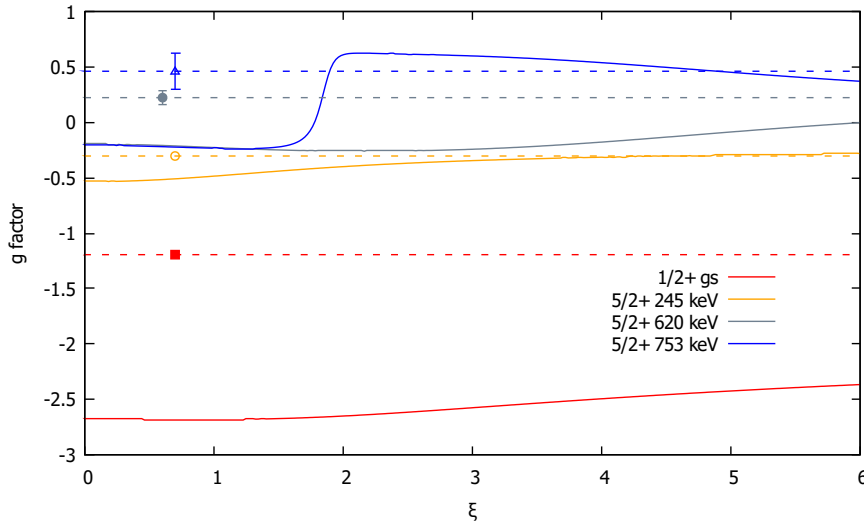


Figure 9.2: Theoretical g factors in the particle-vibration model as a function of the coupling parameter ξ . Experimental results are shown as dashed lines with points to show error values.

The g factor for the 752.8 keV becomes consistent with the experimental result

above $\xi = 2$. However, modifying the coupling parameter does not sufficiently increase the g factor of the ground state. The theoretical g factor of the ground state is found to be insensitive to changes in the coupling parameter. The energy levels were recalculated with a new coupling parameter of $\xi = 2.2$. In order to recover the fit to the level energies the core excitation energy was forced lower, to $\hbar\omega = 440$ keV. The energy levels for these new parameters are displayed in figure 9.1. As the core excitation of the neighbouring ^{112}Cd is 618 keV, lowering the energy to 440 keV in ^{111}Cd does not seem realistic.

It is possible to determine the cause in the change of the g factor for the 752.8 keV state by observing the change in the decomposition of the wavefunction into shell model orbits. The coefficients for the components of the wavefunction for the state of interest are given in table 9.1 for coupling parameters of $\xi = 0.56$ and $\xi = 2.2$. A significant change in character occurs. Initially the state is mostly comprised of the $d_{\frac{5}{2}}$ state coupled to the 2_1^+ core excitation. When the particle coupling parameter is increased, the $d_{\frac{3}{2}} \otimes 2_1^+$ coefficient increases and the state is made of approximately equal amounts of $d_{\frac{3}{2}} \otimes 2_1^+$ and $d_{\frac{5}{2}} \otimes 2_1^+$ states. This is a similar phenomenon to that which occurs to raise the g factor of the ground state in the particle-rotor model as seen in figure 2.2.

Table 9.1: Particle-vibration wavefunction breakdown for 752.8 keV state. As the coupling parameter increases the state changes character from a majority $d_{\frac{5}{2}}$ state to an approximately even $d_{\frac{5}{2}}/d_{\frac{3}{2}}$ admixture.

$J_p \otimes J_c$	Wavefunction coefficients		
	$\xi = 0.56, \hbar\omega = 550 \text{ keV}$	$\xi = 2.2, \hbar\omega = 550 \text{ keV}$	$\xi = 2.2, \hbar\omega = 440 \text{ keV}$
$\frac{7}{2}^+ \otimes 2_1^+$	-0.0041	0.0492	0.0050
$\frac{7}{2}^+ \otimes 2_2^+$	-0.0261	0.2520	-0.1993
$\frac{7}{2}^+ \otimes 4_2^+$	0.0386	0.2286	-0.1204
$\frac{5}{2}^+ \otimes 0_2^+$	-0.0789	-0.0156	-0.0930
$\frac{5}{2}^+ \otimes 2_2^+$	0.0540	-0.1448	0.1221
$\frac{5}{2}^+ \otimes 4_2^+$	-0.0859	0.2522	-0.3297
$\frac{5}{2}^+ \otimes 0_1^+$	0.1357	0.0588	0.2845
$\frac{5}{2}^+ \otimes 2_1^+$	0.9545	-0.3363	0.5833
$\frac{3}{2}^+ \otimes 2_1^+$	-0.0211	0.2199	-0.1832
$\frac{3}{2}^+ \otimes 2_1^+$	0.0172	0.7719	-0.5523
$\frac{3}{2}^+ \otimes 4_1^+$	-0.0182	-0.1838	0.0071
$\frac{1}{2}^+ \otimes 2_1^+$	-0.0071	-0.0390	-0.0680
$\frac{1}{2}^+ \otimes 2_1^+$	0.2250	0.0295	0.2102

9.2 Particle-rotor interpretation

In the particle-rotor model the level structure can be heuristically and naturally explained in terms of the Nilsson orbits and the position of the Fermi level. The deformation parameter can be calculated from the experimentally determined quadrupole moment of the $\frac{5}{2}^+$ state in ^{111}Cd . The quadrupole moment $Q = 0.77(12)$ corresponds a deformation parameter of $\epsilon \sim 0.15$ [Bla09]. The Nilsson orbits expected to be close to the Fermi surface are the $\frac{1}{2}^+[411]$ and $\frac{5}{2}^+[402]$ orbits, with possible low-energy excitations to the $\frac{7}{2}^+[404]$ and $\frac{5}{2}^+[413]$ orbits.

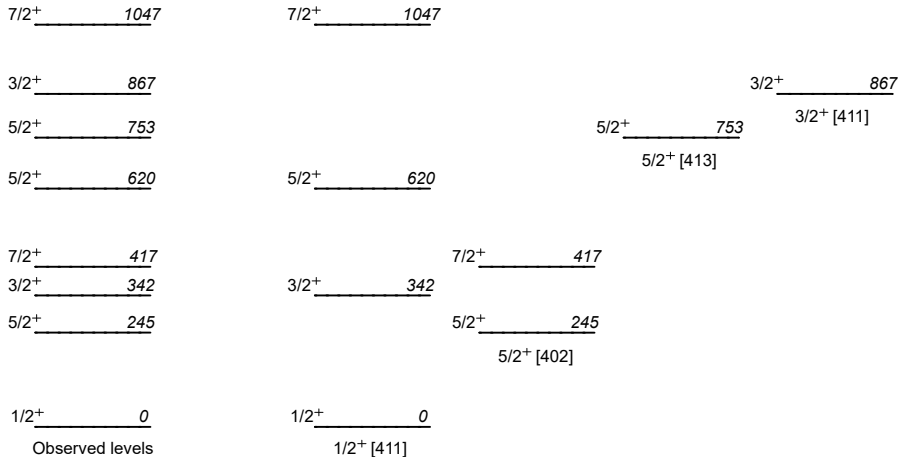


Figure 9.3: Level scheme for the Nilsson based particle-rotor interpretation of the observed level structure.

9.2.1 The ground-state band

The ground state has spin and parity $\frac{1}{2}^+$ and so was identified as the state from an unpaired nucleon in the $\frac{1}{2}[411]$ orbit. The $\frac{3}{2}^+$ and $\frac{5}{2}^+$ states were strongly populated by Coulomb excitation suggesting collective structure. It was shown in section 3.7.2 that the transitions from these states to the ground state have a ratio of $B(E2)$ strengths consistent with identification as members of the ground state rotor “band”. In figure 9.3 the $\frac{3}{2}^+$ and $\frac{5}{2}^+$ have been placed into this band. The observed state at 1046.8 keV has also been tentatively placed in the $\frac{1}{2}[411]$ rotational band. The relatively strong excitation of a high energy $\frac{7}{2}^+$ state from a $\frac{1}{2}^+$ ground state from Coulomb excitation suggests that the state is collective. It must be excited in a multi-step process as Coulomb excitation is an $E2$ process. This process is most likely to occur through states with high excitation cross sections in the same band. This logic is consistent with the 1046.8 keV state being a member of the ground state band, which was the most strongly Coulomb excited band. The other potential identification of this state is the first rotational excitation of the $\frac{5}{2}[413]$ state. This is possible, but unlikely; a multistep Coulomb excitation through a

single particle excitation will occur much less than multistep processes through collective states.

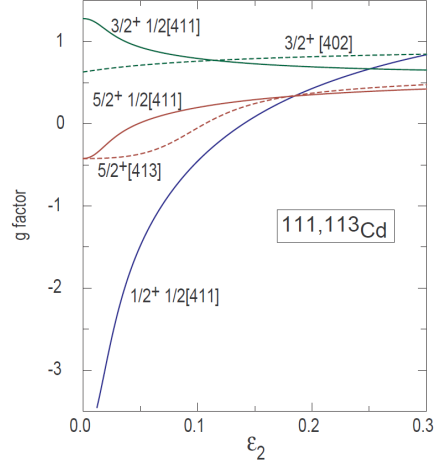


Figure 9.4: Particle-rotor calculation of g factors as a function of quadrupole deformation ϵ_2 . An immediate and dramatic effect is seen in the ground state rapidly raising the g factor as deformation increases.

9.2.2 The 245 keV and 416.7 keV levels

A natural identification of the 245 keV $\frac{5}{2}_1^+$ state in the particle-rotor interpretation is a single particle excitation of the unpaired nucleon into the $\frac{5}{2}[402]$ orbit. The isomeric nature of the state has allowed a precise measurement of the g factor. This has been shown to support the identification of this state as a state with $d_{5/2}$ parentage [Stu16]. In figure 9.5 the $\frac{5}{2}[402]$ and $\frac{5}{2}[413]$ undergo an “avoided crossing”, i.e. the states seem to repel each other in the Nilsson scheme, and hence mix strongly at $\epsilon \sim 0.1$. In this process the $\frac{5}{2}[402]$ orbit can gain much of the $d_{5/2}$ character. In figure 9.4 significant change in the predicted g factor of the $\frac{5}{2}^+[413]$ occurs consistent with mixing between it and the $\frac{5}{2}^+[402]$ orbit. The low-lying isomeric $\frac{5}{2}_1^+$ state with $d_{5/2}$ character is thus a simple prediction of the particle rotor model. The only observed transition from the 416.7 keV $\frac{7}{2}_1^+$ was to the $\frac{5}{2}_1^+$ state; this observation is consistent with data from Nuclear Data Sheets [Bla09]. The connection between these states suggest that the $\frac{7}{2}_1^+$ state belongs to the rotational band of the $\frac{5}{2}[402]$ orbit. A $\frac{9}{2}^+$ state is listed in Nuclear Data Sheets at 987 keV with observed gamma-ray branches to the $\frac{7}{2}_1^+$ and $\frac{5}{2}_1^+$ states and so is likely a member of the rotational band built on the 245 keV $\frac{5}{2}_1^+$ band-head.

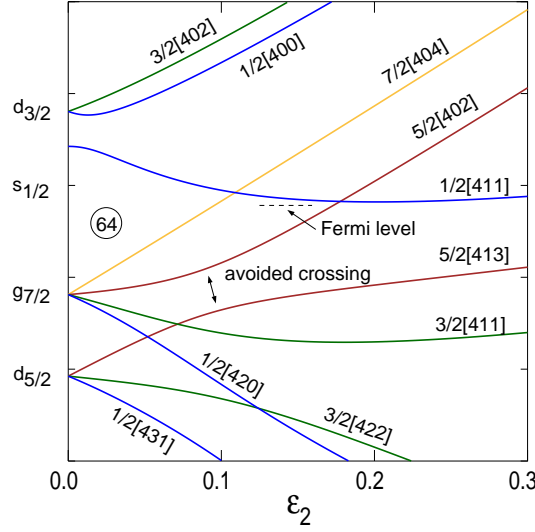


Figure 9.5: Particle-rotor calculation of single-particle energy levels as a function of quadrupole deformation ϵ_2 . The approximate Fermi level is drawn as a dashed line. The $\frac{5}{2}[402]$ and $\frac{5}{2}[413]$ undergo an avoided crossing around $\epsilon_2 = 0.1$ and mixing will occur.

9.2.3 The 752.8 keV state

While the $\frac{1}{2}[411]$ and $\frac{5}{2}[402]$ bands account for all observed low-excitation states, and the absence of a second $\frac{3}{2}^+$ state with collective character, the 752.8 keV state is not expected in these bands. The measured $B(E2; \frac{5}{2}_3^+ \rightarrow \frac{1}{2}_1^+)$ strength of 4.2(13) W.u. [Sin85] is suggestive of collectivity however it is significantly less than for the 342 keV and 620 keV states. The likely explanation of this result is that the 752.8 keV excitation is a mixed state with components related to the $\frac{1}{2}[411]$ band as well as the $\frac{5}{2}[402]$ band. The mixed character of the $\frac{5}{2}_3^+$ state is supported by the observation of strong gamma-ray branches to members of both the $\frac{1}{2}[411]$ and $\frac{5}{2}[402]$ bands. Additionally, by the same process that brought $d_{5/2}$ character to the $\frac{5}{2}[402]$ orbit, the avoided crossing acts to mix the states and can explain the decay to both lower bands.

9.2.4 The 867 keV state

The $\frac{3}{2}_2^+$ state observed at 867 keV has a measured $B(E2) \downarrow$ value of 0.60(22) [Sin85] and was only weakly excited in the present work. This suggests a single particle structure. It has therefore been identified as the $\frac{3}{2}[411]$ single-particle state.

9.2.5 g factors and the Nilsson assignments

The assignments of levels to bands built on Nilsson orbits are consistent with the measured g factors. Importantly, this approach predicts three low-excitation states with

$I^\pi = \frac{5}{2}^+$. The lowest has a negative g factor while the next two have positive g factors, in agreement with experiment. The other levels have been discussed in [Stu16].

Conclusion

The aim of this thesis was to clarify the low-lying level structure of ^{111}Cd , measure the g factors, and characterise the nucleus by reference to the particle-vibration and particle-rotor models. Particle-gamma angular correlations were measured and a spin-parity assignment of $\frac{5}{2}^+$ was confirmed for the contentious 752.8 keV state. The purported $\frac{3}{2}^+$ state at 754.9 keV was not observed. This suggests that the 754.9 keV state has been erroneously introduced into Nuclear Data Sheets. A $\frac{3}{2}^+$ state at this level therefore cannot be due to a collective excitation of the core as this would be strongly Coulomb excited, and hence observed, in this experiment. The non-observation of a second strongly Coulomb excited state near the excitation energy of the 2^+ state of the neighbouring even nuclei is a serious problem for the particle-vibration model interpretation of ^{111}Cd . However, it was shown that many of the observed features can be explained, or at least classified, in terms of a simple particle-rotor model. These include the spins and parities of observed levels, the relative transition strengths between levels, and the g factors of low lying states. Rigorous fitting in this model was not performed as the particle-rotor model is not well developed for nuclei with small deformations. As such, the lack of restrictions on the model parameter space reduces the significance of obtaining an accurate energy fit. Problems may also arise stemming from the deformation changing between different excited states. Further theoretical development in this area should be to further characterise collectivity in weakly deformed nuclei.

In this work transition strengths were not calculated due to the large number of matrix elements to be fitted in the odd- A isotope ^{111}Cd with only a limited number of measured gamma-ray intensities. Further measurements are planned for early-2017 with a larger number of particle detectors in a range of angles. The range of scattering angles allows the dependence of the excitation function to be measured as a function of the interaction strength between the beam and target particles. From such data a comprehensive set of $E2$ matrix elements can be determined [Fah88].

Precision measurements were also made of the g factors of several excited states including a previously unmeasured g factor for the 752.8 keV state. These measurements were compared with the predictions of the particle-vibration model with significant deviations observed. These observations too can be explained with configuration mixing in simple particle-rotor calculations [Stu16].

The inability of the particle-vibration model to predict the low-energy structure and properties of ^{111}Cd suggests that attempting to describe the even-even Cd isotopes with modified vibration models is not the optimal approach.

Bibliography

- [Ald75] Alder, K., et al. The Electromagnetic Interaction In Nuclear Spectroscopy. North-Holland Publishing Company, 1st edition, 1975.
- [BK89] Benczer-Koller, N., et al. Magnetic moments of low-lying states in ^{103}Rh , $^{111,113}\text{Cd}$, and $^{123,125}\text{Te}$. *Phys Rev C*, 40(1), 1989.
- [Bla09] Blachot, J. Nuclear Data Sheets for $A = 111$. *Nucl Data Sheets*, 110(6):1239–1407, 2009.
- [Boh75] Bohr, A. and Mottelson, B. Nuclear Structure: Volume II. W.A. Benjamin Inc., Massachusetts, 1975.
- [Cas90] Castel, B. and I.S., T. Modern Theories of Nuclear Moments. Oxford University Press, Midsomer Norton, 1990.
- [Cha11] Chamoli, S.K., et al. Measured g factors and the tidal-wave description of transitional nuclei near $A=100$. *Phys Rev C - Nucl Phys*, 83(5):1–16, 2011.
- [Cho67] Choudhury, D. and O’Dwyer, T. INTERMEDIATE COUPLING APPROACH (I). Odd-mass Pm nuclei. *Nucl Phys*, 93:300–320, 1967.
- [Eis87] Eisenberg, J. and Greiner, W. Nuclear Models: Volume 1. North-Holland Publishing Company, Amsterdam, 3 edition, 1987.
- [Fah88] Fahlander, C., Bäcklin, A., and Hasselgren, L. Quadrupole collective properties of ^{114}Cd . *Nucl Phys A*, 485:327–359, 1988.
- [Gar10] Garrett, P.E. and Wood, J.L. On the robustness of surface vibrational modes: case studies in the Cd region. *J Phys G Nucl Part Phys*, 37(6), 2010.
- [Geo01] Georgiev, G. Magnetic Moments of Isomers and Ground States of Exotic Nuclei Produced by Projectile Fragmentation. Ph.d. thesis, Katholieke Universiteit Leuven, 2001.
- [Hey83] Heyde, K., et al. Coexistence in odd-mass nuclei. *Phys Rep*, 102(56):291–393, 1983.
- [Hey11] Heyde, K. and Wood, J.L. Shape coexistence in atomic nuclei. *Rev Mod Phys*, 83(4):1467–1521, 2011.

-
- [Koi67] Koike, M. Elastic and Inelastic Scattering of 14 MeV Protons From ^{111}Cd , ^{112}Cd and ^{113}Cd . *Nucl Phys*, 98:209–227, 1967.
- [Kra88] Krane, K. Introductory Nuclear Physics. John Wiley & Sons Inc, 1988.
- [Lam90] Lampard, G. Gyromagnetic ratios of excited states of selected odd-A nuclei. Ph.d. thesis, University of Melbourne, 1990.
- [May55] Mayer, M. and Jensen, J. Elementary Theory of Nuclear Shell Structure. John Wiley & Sons Inc., New York, 1955.
- [Mcd68] McDonald, J. and Porter, D. Excited States in ^{111}Cd . *Nucl Phys*, 109:529–538, 1968.
- [Mes66] Messiah, A. Quantum Mechanics: Volume 2. North-Holland Publishing Company, Amsterdam, 1966.
- [Mor76] Morinaga, H. and Yamazaki, T. In-beam gamma-ray spectroscopy. North-Holland Publishing Company, Oxford, 1976.
- [Row70] Rowe, D.J. Nuclear Collective Motion: Models and Theory. Methuen and Co. Ltd., London, 1970.
- [Row10] Rowe, D.J. and Wood, J.L. Fundamentals of Nuclear Models: Foundational Models. World Scientific, 2010.
- [Sha61] Shalit, A.D. Core Excitations in Nondeformed, Odd-A Nuclei. 122(5):1530–1536, 1961.
- [Sin85] Singh, K.P., et al. Coulomb excitation of cadmium isotopes with protons. *Phys Rev C*, 31(1), 1985.
- [Stu81] Stuchbery, A., Ryan, C., and Bolotin, H.H. Velocity dependence of the transient hyperfine field at Pd ions swiftly recoiling through magnetized Fe. *Phys Rev C*, 23(4):1618–1623, 1981.
- [Stu82] Stuchbery, A. Experimental determinations of gyromagnetic ratios of excited states in $^{196,198}\text{Pt}$ and transient hyperfine field measurements. Ph.D. thesis, University of Melbourne, 1982.
- [Stu98] Stuchbery, A.E., Lampard, G.J., and Bolotin, H.H. Spectroscopy of ^{155}Gd following Coulomb excitation : Signature-independent M1 properties and evidence for octupole correlations. *Nucl Phys A*, 642:361–386, 1998.
- [Stu16] Stuchbery, A., Chamoli, S., and Kibédi, T. Particle-rotor versus particle-vibration features in g factors of ^{111}Cd and ^{113}Cd . *Phys Rev C*, 93(3), 2016.
- [Woo92] Wood, J.L., et al. Coexistence in even-mass nuclei. *Phys Rep*, 215(3-4):101–201, 1992.

Appendices

Clebsch-Gordan coefficients

When coupling systems of angular momentum it is useful to be able to expand a state such that it is an eigenstate of \hat{J}^2 , \hat{j}_1 , \hat{j}_2 , and \hat{J}_z . Here \hat{J}^2 is the total angular momentum operator for the combined system, \hat{j}_1 is the angular momentum operator for the system 1, \hat{j}_2 is the angular momentum operator for the system 2, and \hat{J}_z is the z -component of the angular momentum operator for the combined system [Mes66]. The expansion is given by

$$|JM\rangle = \sum_{m_1=-j_1}^{j_1} \sum_{m_2=-j_2}^{j_2} |j_1 m_1\rangle |j_2 m_2\rangle \langle j_1 m_1 j_2 m_2 | JM \rangle \quad (\text{A.1})$$

where j_1 and j_2 are the angular momenta of the original system, and m_1 and m_2 are the projection of these angular momenta on the z -axis. These couple to angular momentum J and z -projection M . The Clebsch-Gordan coefficients are the expansion coefficients $\langle j_1 m_1 j_2 m_2 | JM \rangle$.

Racah W-coefficients and Wigner 6j-symbols

When coupling three angular momenta it is possible to couple systems in different orders with basis states eigenvectors of either $\mathbf{j}_1 + \mathbf{j}_2$ or $\mathbf{j}_2 + \mathbf{j}_3$. A unitary transformation between these different bases is possible and is performed using Racah W-coefficients as described in Ref. [Mes66]. Coupling three angular momenta j_1 , j_2 , and j_3 with z -projections m_1 , m_2 , and m_3 to angular momentum J and z -projection M it is useful to define the basis states as angular momentum eigenstates of the total angular momentum, the coupled system of two angular momenta and the remaining angular momentum vector, for example

$$|((j_1 j_2) J_{12} j_3) JM\rangle = \sum_{M_{12}=-J_{12}}^{J_{12}} \sum_{m_3=-j_3}^{j_3} |(j_1 j_2) J_{12} M_{12}\rangle |j_3 m_3\rangle \langle J_{12} M_{12} j_3 m_3 | JM\rangle \quad (\text{B.1})$$

or,

$$|(j_1 (j_2 j_3) J_{23}) JM\rangle = \sum_{M_{12}=-J_{23}}^{J_{23}} \sum_{m_1=-j_1}^{j_1} |(j_2 j_3) J_{23} M_{23}\rangle |j_1 m_1\rangle \langle J_{12} M_{12} j_3 m_3 | JM\rangle, \quad (\text{B.2})$$

where J_{ik} and M_{ik} are the coupled angular momentum for j_i and j_k and their z -projection.

Converting from one basis to the other

$$|((j_1 j_2) J_{12} j_3) JM\rangle = \sum_{J_{23}} |(j_1 (j_2 j_3) J_{23}) JM\rangle \langle ((j_1 j_2) J_{12} j_3) J | (j_1 (j_2 j_3) J_{23}) J \rangle. \quad (\text{B.3})$$

The expansion coefficients are independent of M and so M is removed from the symbol. The Racah W-coefficient is defined to be proportional to these expansion coefficients.

$$W(j_1 j_2 j_3; J_{12} J_{23}) = \frac{\langle (j_1, (j_2 j_3) J_{23}) J | ((j_1 j_2) J_{12}, j_3) J \rangle}{\sqrt{(2J_{12} + 1)(2J_{23} + 1)}} \quad (\text{B.4})$$

where

The Racah W-coefficients are related to the Wigner 6j-coefficients by

$$W(j_1 j_2 J j_3; J_{12} J_{23}) = (-1)^{j_1 + j_2 + j_3 + J} \begin{Bmatrix} j_1 & j_2 & J_{12} \\ j_3 & J & J_{23} \end{Bmatrix} \quad (\text{B.5})$$